Quaternary Science Reviews 368 (2025) 109550

Contents lists available at ScienceDirect

Quaternary Science Reviews

journal homepage: www.elsevier.com/locate/quascirev

Close to sunlight or deep underground? New data to reconstruct site formation processes at the Middle Paleolithic Escoural cave (southern Portugal)

Guillermo Alzate-Casallas [a,*], Ana I. Gomes [a,b], Nolan Ferar [a], Sahra Talamo [c], Laura Tassoni [c], João Cascalheira [a], Alvise Barbieri [a]

[a] ICArEHB - Interdisciplinary Center for Archaeology and the Evolution of Human Behavior, FCHS, Universidade do Algarve, Portugal
[b] Centre for Marine and Environmental Research (CIMA)—Infrastructure Network in Aquatic Research (ARNET), Faculty of Science and Technology, Universidade do Algarve, Faro, Portugal
[c] Department of Chemistry G. Ciamician, Alma Mater Studiorum, University of Bologna, Bologna, Italy

ARTICLE INFO

Handling editor: Donatella Magri

Keywords:
Micromorphology
Site formation
Middle Paleolithic
Southern Portugal
Carnivores
Radiocarbon
Geochemistry
Cave
Neanderthals

ABSTRACT

The ability to exploit the deeper levels of cave systems is regarded as complex human behavior. Evidence that Neanderthals possessed this skill remains limited. The site of Escoural, in southern Portugal, is worldwide renowned for the Upper Paleolithic rock art that was performed in the lowermost level of the cave. The site also preserved Middle Paleolithic sequences in a deep chamber (P1) as well as in an area that today lies outside of the cave (P2). Due to the lack of geoarchaeological analyses, it is currently impossible to clarify whether these materials reflect systematic Neanderthal visits to these site areas. In this study we integrated geoarchaeological data and radiocarbon dating to (i) reconstruct site formation processes, and (ii) explore the interaction between Neanderthals and carnivores at Escoural.

Micromorphological, stratigraphic, and geochronological results demonstrate that colluviation moved sediments and archaeological finds from upper cave chambers into P1. This process likely mixed separate and distinct assemblages, possibly leading to co-occurring high concentrations of carnivore coprolites and lithic artifacts. In contrast, P2 preserves in situ Neanderthal occupations alternating with carnivore visits. Neanderthal foragers used this area when it was a large chamber located close to the original cave entrance, which was subsequently lost due to roof collapses and likely impacted by modern quarrying activities.

These findings align with broader Eurasian patterns indicating that Neanderthals primarily used well-lit karstic cavities rather than deep, enclosed spaces. Moreover, this study underscores that post-depositional processes may have profound impacts on our interpretation of Neanderthal and carnivore cave use.

1. Introduction

Few exceptions aside (Jaubert et al., 2016; Pitarch Martí et al., 2021), vast evidence from Eurasia has led to the interpretation that Neanderthals seldomly used the deep chambers of karst systems, while they preferred to exploit cave entrances, rock shelters, and open-air sites (Conard et al., 2012; Ekshtain et al., 2019; Moclán et al., 2023; Münzel and Conard, 2004). This trait of Neanderthal cave use has been interpreted, not without criticism (Jaubert et al., 2016), as indicative of lower population density and somewhat more limited cognitive abilities than their *H. sapiens* successors (Conard, 2010; Mellars, 1989; Mellars and French, 2011; Villa and Roebroeks, 2014). Investigating Neanderthal use of karstic spaces is an important avenue for further exploring their settlement strategies. Furthermore, it can provide important data to unveil their site maintenance practices as well as their interaction with other cave nesters, such as hyenas, cave bears, and birds (Blanco et al., 2021; Buccheri et al., 2016; Discamps et al., 2012; Finlayson et al., 2012).

Studying the use of karst by Neanderthals, however, can be challenging due to the extensive post-depositional transformations that cave environments undergo (Barbieri, 2019; Butzer, 2008; Ford and Williams, 2007; Goldberg and Mandel, 2008; Goldberg and Sherwood,

* Corresponding author.
E-mail address: gacasallas@ualg.pt (G. Alzate-Casallas).

https://doi.org/10.1016/j.quascirev.2025.109550
Received 20 March 2025; Received in revised form 20 June 2025; Accepted 26 July 2025
Available online 1 August 2025

2006; Karkanas and Goldberg, 2013; Mallol and Goldberg, 2017; White, 2007). Over millennia, processes such as carbonate dissolution, structural collapses, erosion, and mass wasting might have significantly altered the original stratigraphy and spatial organization, moving archaeological materials and sediments closer to the ground surface or burring them deeper into the karst (Bosch and White, 2004; Gillieson, 2021). These transformations generally follow two major pathways.

First, roof collapses and other structural instabilities may drastically alter the internal morphology of caves, fragmenting once-continuous occupation surfaces and creating stratigraphic inversions or discontinuities. Several well-documented examples illustrate this phenomenon. At Lezetxiki II in northern Iberia, a major collapse during the early Upper Pleistocene divided the sequence into a deep cave and a shallower rockshelter context (Arriolabengoa et al., 2018). Similar taphonomic shifts occurred at El Castillo (Martín-Perea et al., 2023), Arbreda (Lozano et al., 2024), Gruta da Oliveira (Angelucci et al., 2023), Navalmaíllo (Moclán et al., 2023), and Figueira Brava (Cardoso and Cascalheira, 2024; Zilhão et al., 2020), where roof collapses redefined the spatial accessibility and preservation of archaeological deposits.

Second, colluviation and other sedimentary processes can lead to the post-depositional displacement of archaeological materials from their original place of deposition. In such cases, assemblages originally located near cave mouths or external platforms may be relocated deeper into karst systems through slope wash, gravity-driven flow, or debris movement. This has been clearly demonstrated at sites like La Ferrassie (France), where geoarchaeological studies revealed that many artifacts and faunal remains in the cave's interior were actually reworked downslope from an elevated platform located several meters away (Aldeias et al., 2023). Similar processes have been documented at Pech de l'Azé IV (Goldberg et al., 2012), Kebara (Goldberg et al., 2007), Companheira (Barbieri et al., 2023) and Gruta da Oliveira (Angelucci and Zilhão, 2009) where slope-derived colluvial deposits significantly affected the spatial and stratigraphic integrity of archaeological layers.

In this paper, we investigate a karstic system that underwent both types of transformations—Escoural Cave (Montemor-o-Novo), in southern Portugal. The site is renowned for its Upper Paleolithic rock art, which was discovered in the deepest chambers of the cave, as well as for its stratified Middle Paleolithic deposits, which were also unearthed in a deep chamber as well as in an area that today lies outside of the cave system (Otte and Silva, 1996). So far, no analysis was conducted to establish whether Middle Paleolithic deposits at the site are preserved in situ, making it impossible to conclude which area of the site was actually exploited by Neanderthals. Our study aims to (i) clarify which site areas were more likely occupied by these hunter-gatherers and (ii) explore the potential competition for space between them and carnivores. To address these questions, we applied an integrative geoarchaeological framework that combines soil micromorphology, geochemical analysis, and radiocarbon dating. This research enhances our understanding of the cave's stratigraphy and occupation history, offering valuable insights into Neanderthal use of karstic spaces and their role in settlement dynamics.

2. The site

Escoural is a dolomitic cave located about 15 km south of Montemor-o-Novo (Alentejo, Southern Portugal) and 3 km east of Santiago do Escoural. The cave extends north-south and comprises a main hall (Gallery 1) connected to 18 smaller cavities (Fig. 1a–b). It is the sole cave within a 50-km radius and the only karst system in interior Alentejo. Escoural is also Europe's westernmost cave with Paleolithic rock art and the only one in Portugal (Lopes, 2013). Naturally protected and strategically positioned at the edge of the Monfurado mountain, it offers a wide view over surrounding plains, providing a privileged vantage point for control landscape and hunting game (Peyroteo-Stjerna et al., 2018).

The region experiences a Mediterranean climate with continental influences, characterized by hot, dry summers and mild, wet winters. Annual precipitation is low, averaging 400–600 mm, from October to March. Summer temperatures often exceed 30 °C, while winter temperatures rarely drop below 5 °C (Barquín, 2015; IPMA, 2022; Malaurent et al., 2004).

Geologically, Montemor-o-Novo County is made of Precambrian and Pliocene metamorphic rocks like schist, shale, mica schist, amphibolite shale, and gneiss (Araújo and Lejeune, 1995; Carvalhosa, 1989; Peyroteo-Stjerna et al., 2018; Vegas, 1968). The karstic system of Escoural developed along a narrow fault of crystalline limestones, which metamorphic processes locally recrystallized in dolomite and marble with hornfels and gneiss intercalations. Approximately 600 m west, the Geological Map of Portugal (LNEG, 2024), indicates the presence of the Complexo Vulcano-Sedimentar de Moura–Santo Aleixo, specifically the Xistos de Moura unit, which comprises Ordovician–Silurian basic volcanic and volcano-sedimentary rocks.

2.1. Previous archaeological excavations of S3(A-B) and S4

The site was discovered in the early 20th century by local marble quarry workers who breached the main hall, sealed since Prehistory due to its collapsed original entrance (Otte and Silva, 1996). Manuel Farinha dos Santos led the first excavations (1960s–80s), uncovering Middle Paleolithic materials in the southernmost galleries, outside the cave, and a narrow passage connecting these two areas (Fig. 1b–d) (Dos Santos, 1964). These investigations also revealed *Homo sapiens* visits, evidenced by parietal paintings and engravings in Gallery 1, likely from the Solutrean (22,000–17,000 BCE) and Magdalenian (18,000–10,000 BCE) (Hruban, 2019). During the Holocene, Neolithic groups (c. 5500–3000 cal BCE) buried their dead inside the cave, while Chalcolithic people (3000–2500/2750 BCE) settled on the plateau above it (Gomes et al., 1983, 2012; Hruban, 2019; Peyroteo-Stjerna et al., 2018).

Further research (1989–92) by Marcel Otte and António Carlos Silva (Otte and Silva, 1996), focused on areas previously explored by Dos Santos, confirming the sole presence of Upper Paleolithic deposits in Gallery 1. Additionally, they expanded the excavation of Middle Paleolithic deposits in the deeper chamber formed in the southern part of the cave, Gallery 18, as well as in an area that is today located outside of the cave, *Sondagem* 4 (S4). Excavations used 10 cm spits, recording main finds with *x*, *y*, and *z* coordinates. In Gallery 18, Sondagem 3 (S3) and its extensions (S3A–B) covered approximately 2 m^2, exposing a 230 cm sequence that yielded exclusively Middle Paleolithic stone tools. The assemblage is dominated by local hydrothermal quartz (99 %), accompanied by smaller quantities of quartzite, flint, and sandstone, and includes Levallois flakes in limestone and black siliceous rock. The toolkit reflects simple reduction strategies, including unprepared "globular" cores with multidirectional, unorganized removals, and "parallelepiped" cores characterized by orthogonal removals. The latter take advantage of natural ridges that naturally occur on angular pieces of the local hydrothermal quartz. Prepared discoidal and Levallois quartz cores are present in smaller quantities. Few retouched flakes were identified (Otte and Silva, 1996). Carnivore coprolites and faunal remains were found, including a horse tooth from Layer 5 (80–90 cm depth) dated by U-Th to 48.9 ± 5.8 ka BP (Otte and Silva, 1996). Given the confined space (3.2 × 6.5 m), the excavators suggested that the assemblages might not reflect in situ Neanderthal occupations but could have been reworked from S4 by colluviation (Otte and Silva, 1996).

In S4, Otte and Silva (1996) excavated 15 m^2 to a depth of 5 m (Fig. 1b and d), identifying six stratified deposits. The upper section (Layer 1A–C) contained large limestone boulders, as well as Neolithic and Chalcolithic artifacts, likely resulting from cave collapse and subsequent infilling with materials derived from the well-known late prehistoric occupations located outside the cave at the top of the hill. Layer 2, the uppermost cave sediment, was correlated with S3's upper layers 1 and 2. Layers 3 and 5 showed bioturbation, while Layer 4, with limestone fragments, faunal remains, and Mousterian quartz tools, was

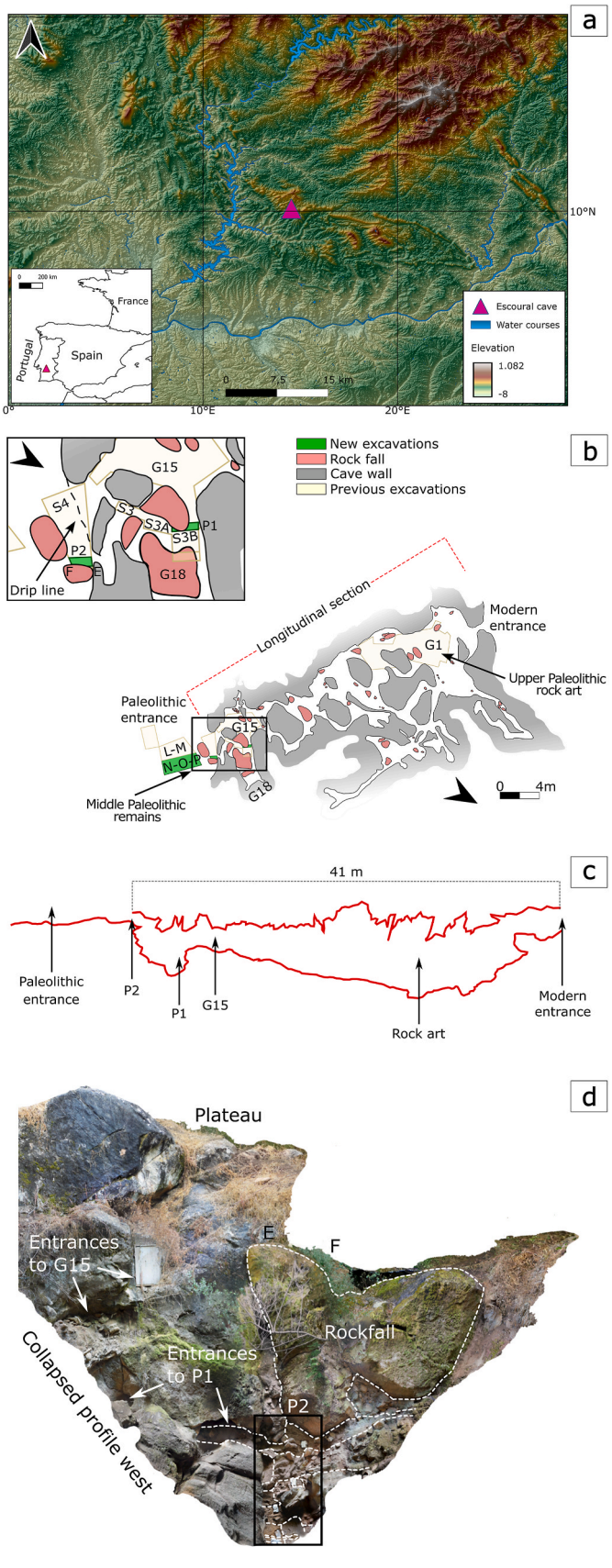

(caption on next column)

Fig. 1. a) Location of the Escoural cave in southern Portugal. **b)** Planimetry of the cave which shows the areas excavated in the 1990s and our team's archaeological campaigns: Profile 1 (P1) and Profile 2 (P2), the longitudinal section depicted in (c), as well as previous excavations, such as *Sondagem* 3 (A–B) and *Sondagem* 4 (S4). **c)** Longitudinal section of the cave displaying the topography, providing an alternative view of the cave's structure. Adapted from GDH-Afrika (2020). **d)** Composite orthophotos from the area outside the cave showing P2 (black square), the entrances to P1, and the major rockfall covering the sequence (E and F).

considered the best-preserved cave deposit. Layer 6 was linked to burrowing activity. The dips of Layers 2–6 suggest Pleistocene sediment inputs from the south, indicating the cave extended further in that direction, though modern quarrying complicates verification (Otte and Silva, 1996).

2.2. Renewed archaeological research

More recently, our team commenced new investigations at the site. We re-investigated S3B and S4 to better understand the formation and chronology of the Middle Paleolithic deposits (Fig. 2a). In S3B, we excavated, moving back by 30 cm, the south profile of the previously dug test pit. We refer to this new excavation as P1 (Fig. 2b). In S4, our team cleaned the exposed profiles and opened a 50 × 50 cm test pit in the eastern corner of the previous trench, deepening the bottom of the excavation by 30 cm without reaching bedrock (Fig. 2c). In this article, we refer to the deepened east profile of S4 as P2. In both excavations, we removed deposits in 10 cm spits while following the natural stratigraphy, stopping the spit if the contact with a geological layer (GL) was encountered before reaching 10 cm. The positions of all finds larger than 2 cm were recorded with a total station. During this campaign, P1 and P2 were sampled for micromorphological study, geochemical analysis, as well as radiocarbon dating.

3. Material and methods

3.1. Sediment profile description

We documented the lithological characteristics of the GLs exposed in P1 and P2. For each GL, we recorded depth, the nature of the transition to the underlying sediment, following Patrick (1980), and the proportions of coarse (>2 mm) and fine (<2 mm) fractions, estimated using frequency charts (Larsen and Chilingarian, 2010). For the fine fraction, we assessed Munsell color and grain size through tactile analysis (Vos et al., 2016). Gravel attributes were detailed by noting color, composition, frequency (Larsen and Chilingarian, 2010), size (based on ISO 14688–1:2002), shape (Zingg, 1935), roundness (Powers, 1953), and sorting (Stoops, 2020). Detailed lithological descriptions are presented in Supplementary Material (SM) 1, available at our online research compendium: www.doi.org/10.17605/OSF.IO/3A8DK.

3.2. Micromorphology

We collected 11 undisturbed sediment blocks from P1 and P2 (Fig. 2), yielding 24 petrographic thin sections. Although we aimed for continuous coverage of both sequences, the lithology of the stratigraphic profiles posed some challenges to our sampling strategy. In P1, GL6 was not sampled because it was extensively cemented. While in P2, GLs 1A-C, 1E-G, 3 and 5 were not sampled due to high amounts of limestone gravels and blocks, and cementation.

All block samples for this study were extracted from the profiles with the help of plaster bandages. The samples were dried in an oven at 40 °C for three days, impregnated with a mixture of resin (70 %), styrene (30 %) and hardener (7 %), and consolidated for about two weeks in the fume hood. Once hardened, the impregnated blocks were cut with a rock saw into chips measuring 50 × 75 mm, which were produced into 30

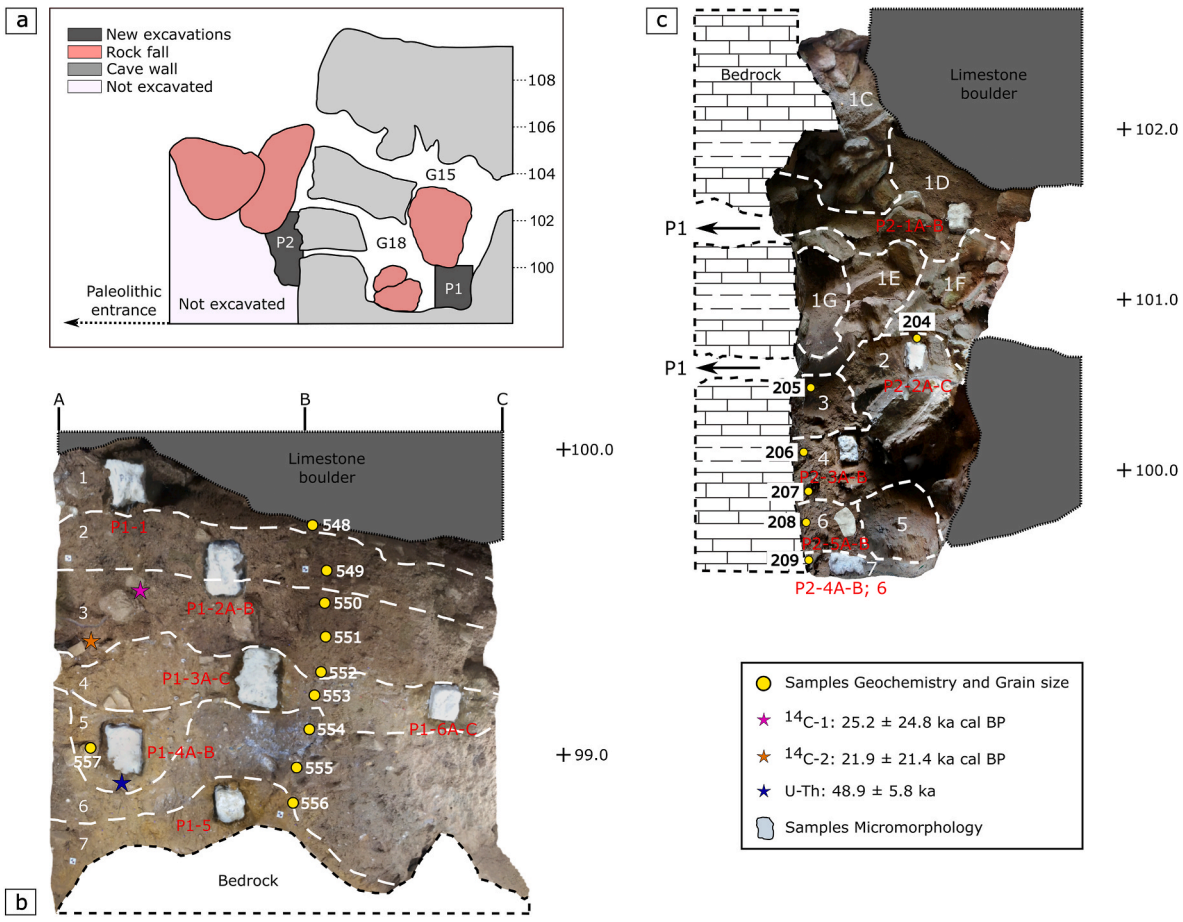

Fig. 2. a) Illustrative sketch depicting the location of P1 and P2 within the karst system. (b) and (c) show stratigraphic profiles indicating the locations of micromorphological block, loose sediment, radiocarbon, and U-Th samples: **b)** North (A–B) and west (B–C) sections of P1, inside the cave. **c)** P2 outside the cave.

μm-thick thin sections. The thin sections were scanned on a flatbed scanner at 1200 dpi in reflection mode. The slides were studied under stereoscopic and petrographic microscopes at magnifications from 5 to 200X, under plane (PPL), cross-polarized (XPL), and Oblique Incident Lights (OIL).

Fluorescence microscopy complemented identification of coprolites, heated/fresh bones, apatite rims, and phosphatic crusts. The equipment used was a Zeiss AxioImager-M2 fluorescent microscope with a motorized plate, an Axiocam 208c for Transmitted Light -TL- and an Axiocam 705 for fluorescence. The filter cube used was a 38 HE eGFP for Blue Fluorescence with a wavelength range of 500–550 nm. The pictures were obtained with the software Zen version 3.4.91.

Identification, terminology, and description of micromorphological features were made based on Stoops (2020), as well as other relevant literature (Goldberg et al., 2001; Goldberg and Macphail, 2006; Karkanas and Goldberg, 2018; Macphail and Goldberg, 2017; Nicosia and Stoops, 2017; Stoops et al., 2010). We conducted a semi-quantitative assessment of thin sections following Friesem et al. (2022) and Brancaleoni et al. (2024) to analyze the relative abundance of sediment components, including phosphatic crusts, calcification features, charcoal, lithics, bones (heated and unheated), coprolites, slope reworking features (rounded sediment aggregates, galaxy and arcuate features, and coatings of dense silty clays with a speckled b-fabric), bioturbation features (bioporosity, passage features and localized mite excrements), Fe-Mn nodules and Fe-rich micro-lenses.

Additionally, we performed a quantitative analysis using manual point counting of coprolites under a petrographic microscope (Loaiza et al., 2015; Stoops, 2020). This method, however, may overestimate coprolite abundance due to fragmentation of larger, weathered specimens. To mitigate this bias, we supplemented the analysis with micro-XRF elemental mapping, enhancing the detection of biogenic byproducts (i.e., phosphates). Despite its limitations, manual point counting remains valuable for assessing the accumulation and spatial distribution of biogenic material, aiding in the interpretation of site formation processes and distinguishing biological activity from other depositional agents.

3.3. Micro X-ray fluorescence (μ-XRF)

All thin sections were analyzed to obtain elemental mappings at the Centro de Instrumentación Científico Técnica (CICT) of the University of Jaén (Spain). The equipment used was a Bruker M4 Tornado, and mappings were conducted for the following elements: Al, Ca, Cu, Fe, K, Mg, Mn, Na, P, S, Si, Ti, and Zn. Beam power of 30 W (tube voltage of 50 kV and tube current of 600 μA), the use of both detectors, a spot size of ~20 μm, and a spot spacing of 25 μm under 20 mbar pressure. Total analysis time per thin section was 09:00 h, at a speed of 5.0 mm/s. Elemental maps were analyzed qualitatively and quantitatively (SM2). Quantification was averaged in layers with multiple thin section, and average deviation was calculated.

Micro-XRF was compared with geochemical data to enhance findings. Despite differing sampling methods, overall data showed strong correlation. This approach was valuable in layers lacking micromorphology samples, offering broader chemical distribution interpretation.

3.4. Geochemical, pH, and grain size analysis

Sediment samples were collected at 10 cm intervals along P1 and P2

(Fig. 2b–c) to cover the Paleolithic layers inside and outside the cave and complement micromorphological analysis. In P1, sampling covered the entire stratigraphic sequence based on previous U-Th dating, and lithic analysis, which suggested that the whole profile includes Paleolithic human input. In P2, sampling focused on the Paleolithic sequence, guided by the stone tools recovered during our work.

Samples were subdivided for elemental analysis (carbon, hydrogen, and nitrogen – CHN), lithogeochemistry, whole rock analysis, and sediment pH determination (SM3). For elemental analysis, sediment subsamples were freeze-dried, milled, and homogenized in a Fritsch Agatha mill. Each subsample was divided into two aliquots. One of the aliquots was placed in a muffle at 500 °C to eliminate the organic content. The total carbon and nitrogen, as well as the inorganic carbon (i.e., CaCO3), were determined through gas chromatography using a Carlo Erba, model EA1108 at the Center for Marine Sciences (Universidade do Algarve). Total organic carbon (TOC) was determined as the difference between total carbon and inorganic carbon (TIC).

The organic carbon and nitrogen ratio (C/N) was used as a proxy for the origin of the organic matter (CSIRO, 2000). C/N values below 10 are indicative of the presence of organic matter rich in proteins (Jover et al., 2014; Meyers, 1997), such as animal feces or guano (Forbes et al., 2007), bones and microorganisms (Benedetti et al., 2019; Finlay and Kendall, 2007; Gleixner, 2013; Peterson and Fry, 1987). Lithogeochemistry and whole rock analysis were carried out at Activation Laboratories Ltd. in Ancaster, Canada, by inductively coupled plasma optical emission spectrometry (ICP-OES; package 4B), providing the concentration of the major oxides (SiO_2, Al_2O_3, Fe_2O_3(T), MnO, MgO, CaO, Na_2O, K_2O, TiO_2, P_2O_5) and trace elements (Ba, Sr, Y, Sc, Zr, Be), as well as the Lost On Ignition (LOI). LOI was measured gravimetrically after heating samples to 550 °C, representing the combined amount of organic matter, hydrated mineral phases, and carbonate in the sediment (Craft et al., 1991).

For grain-size analysis, subsamples were cleaned of organic content using 33 % H_2O_2. As the samples contained both coarse and fine fractions, they were separated using a 2 mm mesh sieve. The fraction >2 mm was dry-sieved, while the <2 mm fraction was analyzed using a Malvern 3000 laser diffraction particle size analyzer. The results from both methods were processed using GRADISTAT, version 8.0 (Blott and Pye, 2001) (SMs 4 and 5). pH was measured potentiometrically in distilled water using a 1:2.5 sediment-to-water ratio, following ISO 10390:2005. Graphical representation of sediment texture, pH, and geochemical data was done using TILIA, version 3.0.3 (Grimm, 2022).

3.5. Vertical analysis of human vs carnivore inputs

To differentiate carnivore and human visits to the site, we integrated geochemical analysis and coprolite point counting in thin sections (Loaiza et al., 2015; Stoops, 2020) with archaeological excavation data. Due to unsystematic recording of find locations by Otte and Silva (1996), we exclusively utilized archaeological data from our excavations.

Carnivore coprolite counts and excavated faunal bones served as proxies for carnivore presence, while lithic artifacts indicated human activity. Micromorphological data were assessed to distinguishing between in situ and reworked materials, providing nuanced understanding of depositional history.

A Spearman's rank correlation test was employed to assess statistical relationships between carnivore and human activity indicators in P2 and P2. We compared coprolite relative abundance with proportions of lithic artifacts and faunal bones per layer. Separate analyses were conducted for P1 and P2 using R version 4.2.3 and the cor.test() function from the stats package. Full results and input data are available in SM6.

3.6. Radiocarbon dating

We selected 11 faunal bones from different P1 layers for radiocarbon dating. However, only two samples belonging to Layer 3 were successfully dated due to low collagen yield (SM7). Sample 218 was a cranium fragment, 270 a vertebra, both from medium-sized mammals. In addition, we attempted to date two faunal bones from GL4 in Profile 2 (P2-196 and P2-203). However, both samples yielded 0 % collagen and could not be dated.

Samples were pretreated following the standard procedure described by Talamo et al. (2021). The samples underwent an 'acid-base-acid' (ABA) treatment designed for decalcification, decontamination, and gelatinization of bone fragments. The process began with immersion in hydrochloric acid (HCl 0.5M), which dissolved the mineral components and some organic contaminants.

Once the CO2 effervescence ceased, the demineralized samples were rinsed once with ultrapure Milli-Q water before being treated with sodium hydroxide (NaOH 0.1 M) for 30 min at room temperature. Following this step, the NaOH solution was replaced with ultrapure water for an additional rinsing phase. The water was then removed, and the samples were re-acidified with HCl 0.5M for another 15 min at room temperature.

To extract collagen, the demineralized bone fragments were subjected to gelatinization using a heater block. This step involved heating the samples in acidic water (HCl pH 3) at 70 °C for 20 h, allowing the collagen to dissolve and form gelatine. The gelatine was then filtered using Eeze-filters to remove small particles (>80 μm), followed by ultrafiltration to separate low-molecular-weight contaminants and degraded proteins (<30 kDa) from the larger molecules (>30 kDa). To minimize contamination risks associated with filter membranes, the Eeze-filters and ultrafilters were thoroughly pre-cleaned before use.

After ultrafiltration, only the >30 kDa fraction was preserved, frozen for 24 h, and subsequently freeze-dried for 48 h. The resulting collagen was then graphitized at the BRAVHO laboratory (Tassoni et al., 2024), using Elemental vario ISOTOPE select in combination with the AGE 3 Automated Graphitization Equipment (IonPlus AG, Switzerland) (Wacker et al., 2010a). The resulting graphite targets were sent to the Curt-Engelhorn-Center for Archaeometry in Mannheim, Germany (CEZA, lab code: MAMS) and measured using a MICADAS AMS (Kromer et al., 2013).

To ensure quality control, a background bone sample with a radiocarbon age exceeding 50,000 years was processed alongside the study samples. This allowed for the detection and correction of any potential contamination introduced during laboratory procedures.

Radiocarbon data reduction was carried out using BATS software (Wacker et al., 2010b), with an additional 1 ‰ error margin applied to the samples in accordance with standard practice. Radiocarbon ages, expressed in 14C years before present (14C BP), were calibrated using OxCal 4.4 (Bronk Ramsey, 2009) and the IntCal20 calibration curve (Reimer et al., 2020). The calibrated age ranges, reported in calibrated years before present (cal BP), are provided with both 1σ (68.3 %) and 2σ (95.4 %) probability intervals. Uncalibrated 14C dates are presented with their respective 1σ uncertainties.

4. Results

4.1. Profile 1 (inside the cave)

4.1.1. 2020's excavation results

In P1 we identified 7 geological layers (GL) (Table 1). Our GLs largely correspond to those previously identified by Otte and Silva (1996). Our team recovered 206 lithic artifacts and 197 faunal bones from P1, recorded with total station. A significant amount of mesofauna remains was also recovered from sieve bags. In GL1, 2 faunal bones (1.02 %) were recorded, while no lithic artifacts were unearthed. GL2 yielded 69 bones (35.20 %) and 8 lithics (3.13 %). In GL3, 66 bones (33.67 %) were identified along with 44 lithics (17.19 %). GL4 contained 54 bones (27.55 %) and 75 lithics (29.30 %). GL5 had 4 bones (2.04 %) and 36 lithics (14.06 %). In GL6, 1 bone (0.51 %) and 72 lithics

Table 1
Summary of field description of the layers and associated micromorphology thin sections of P1.

Layer	Thin section	Field description
GL1	P1_1	Silty sand, crumbly, with roots and burrows. Limestone gravel from fine to medium-sized.
GL2	P1_2A	Sandy silt slightly more compact than GL1.
GL3	P1_2B	Sandy silt, the contact with the above layer is clear. Slightly more compact, and richer in coarse sand and fine gravel than GL2.
GL4	P1_3A-C, 6A-C	Sandy silt with fine to coarse sand of white and yellow limestone, as well as some stacked lenses of carbonate cementation.
GL5	P1_4A-B	Sandy silt, laminated deposit.
GL6	N/A	Sandy silt with rare fine and medium sand of white calcite.
GL7	P1_5	Sandy silt with rare coarse sand of white and yellow calcite. And rare coarse and medium sand-sized mottles.

(28.13 %) were recovered. GL7 yielded no faunal bones and 21 lithics (8.20 %).

Preliminary lithic analysis aligns with previous findings (S3, S3A-B). Except for one flint flake, all lithic artifacts are made of hydrothermal quartz, varying in texture from coarse to very fine-grained, and in colors from milky white to translucent greys and blues. Only 3 retouched artifacts were identified. The cores (n = 4) correspond to the globular and parallelepiped types identified by Otte and Silva (1996). Some preliminary findings are at odds with those of previous works, though these differences may simply be due to the small sample size of the recently excavated materials. Most notably, no discoidal or Levallois cores have been identified, and preserved platforms show little to no evidence of preparation. Of the 44 complete flakes recovered, only three centripetal dorsal removals could attest to discoidal or Levallois reduction. Lastly, some flakes present evidence of the bipolar-on-anvil technique. Furthermore, no archaeological materials diagnostic for the Upper Paleolithic were found in this sequence.

Faunal analysis of the bones recovered from GL 2 in Profile 1 revealed that the assemblage is dominated by rabbit remains, which exhibit extensive tooth marks and digestive damage (Cobo-Sánchez et al., 2024). These findings suggest that carnivore activity was the primary agent of accumulation in that GL. The analysis of bones from the other GLs is in progress, and we expect that also these faunal remains were mostly accumulated by carnivores.

4.1.2. Radiocarbon dating

Of the 11 faunal bone samples selected from GLs 2,3,4 and 5 of Profile 1, only two—both from Layer 3—yielded sufficient collagen for successful ^{14}Cdating (Table 2). The remaining samples yielded collagen contents ranging from 0 % to 1 %, far below the threshold typically required for reliable AMS dating.

Sample P1-218, a cranium fragment of a medium-sized mammal, produced an uncalibrated radiocarbon age of 20,751 ± 50 BP, corresponding to a calibrated range of 25,230–24,860 cal BP (95.4 % probability). Sample P1-270, a vertebra of a medium-sized mammal, returned a radiocarbon age of 17,868 ± 40 BP, calibrating to 21,930–21,440 cal BP (95.4 % probability). These samples yielded stratigraphically inverted results.

4.1.3. Micromorphology and μ-XRF

GL7, the lowermost layer, is observed in thin section P1-5. It is a matrix-supported sediment dominated by silty clay (48.7 %), sand (27 %), and gravel (24.3 %) of quartz, quartzite, and rare limestone. Most of the sedimentary components are geogenic, despite few biogenic and anthropogenic input such as coprolites (5 % of the coprolites identified in the thin sections from stratigraphic sequence, based on point counting), phosphatic nodules, fresh roots, and stone tools (Table 3).

The coprolites we identified microscopically at Escoural are related to either hyena or lynx carnivores, as indicated by diagnostic features such as their rounded to sub-angular shape, pale-yellow to greyish-white color in PPL (Fig. 3a; SM8), the presence of gas vesicles (Fig. 3a), undifferentiated b-fabric in XPL (Fig. 3b), inclusions of mineral grains (Fig. 3b), calcitic pseudomorphs related to hair fibers (Fig. 3c), digested/chewed bones (Fig. 3d–f; SM8) and a darker brown rim (Fig. 3e) (Barbieri and Miller, 2019; Carrión et al., 2001; Courty et al., 1989; Goldberg and Nathan, 1975; Horwitz and Goldberg, 1989; Linseele et al., 2013; Morley, 2017; Morley et al., 2019; Rodríguez et al., 1995; Sanz et al., 2016; Varis et al., 2022). This interpretation agrees with results from previous excavations at the site which yielded numerous hyena coprolites (Otte and Silva, 1996), as well as the study of the part of the faunal bones from P1 by Cobo-Sánchez et al. (2024).

Furthermore, we observed a chaotic microstructure with rounded aggregates and coarse sediment fraction—including bone fragments, coprolites, quartz, and limestone (Fig. 4a). Among these, the quartz grains display angular to subangular edges, indicative of limited mechanical transport. Additionally, we identified sediment aggregates with different matrix compared to the surrounding deposit (SM8), further supporting a model of colluvial sediment influx into the Escoural system (Angelucci and Zilhão, 2009; Bertran, 1993; Bertran and Texier, 1999; Boschian, 1997).

GL5 is localized in the south part of the sequence, displaying a concave morphology. It is a geogenic deposit, matrix-supported, dominated by sand (44.1 %) and silt (35 %) of quartz and some quartzite, moderately sorted, with rough angular to subangular edges. The concentration of gravel (18.9 %) is lower compared to GL7. In GL 5, we observed metamorphic rock fragments exhibiting an inclination of 45° towards the east (SM8). This layer presents rounded aggregates comprising quartz grains and Fe-Mn nodules. Some of the aggregates are coated by circular and arcuate alignments of silt- and sand-sized grains of quartz, which is typical of turbate structures (Fig. 4b; SM8) (Phillips, 2006). In this layer, bones and lithics are more frequent than in the layers below, while carnivore coprolites are rarer (1 % based on counting in thin section).

GL4: In our excavation this layer showed the highest input of human and carnivore activity, containing 82 % of carnivore coprolites (based on point counting in thin sections) and 29 % of stone tools (of all recovered lithics in P1). Field observations revealed laminations, including calcium carbonate crusts. Micromorphological analysis identified three distinct micro-layers within GL4 (A-C), all matrix-supported but with compositional differences.

GL4A, located at the base and in contact with GL6, forms a subhorizontal lamination 2.5–5 cm thick (Fig. 4c–f; SM8), sloping towards the east. This micro-layer is characterized by a speckled b-fabric with phosphatized or decalcified clayey and silty to sandy groundmass. Additionally, we identified two types of laminations made from: (i) discrete Fe-rich micro-lenses displaying grain size grading, and (ii) silt to fine sand within a yellowish clayey matrix (4A1 and 4A2 in Fig. 4c–d).

μ-XRF elemental mapping revealed a high degree of phosphatization in GL4A. However, only a few coprolites were identified, and those are highly fragmented. The groundmass composition of this centimetric

Table 2
AMS radiocarbon dating of bone samples from Profile 1.

Field code	Lab n° MAMS	Lab code	^{14}C age (yr BP)	±	δ13C AMS (‰)	Probability 68 %	Probability 95 %	Material
P1-218	74503	BRA-7103	20751	50	−24.3	25140-24970 cal BP	25230-24860 cal BP	Graphite
P1-270	74504	BRA-7105	17868	40	−22.8	21880-21480 cal BP	21930-21440 cal BP	Graphite

Table 3
Representative micromorphological features in micromorphology thin sections at Escoural. (- not seen; * few; ** common; *** dominant). Based on Friesem et al. (2022) and Brancaleoni et al. (2024). Abbreviations: **PF**: Profile; **TS**: Thin Section; **LY**: Layer; **PHC**: Phosphatic Crust; **CA**: Calcification; **CH**: Charcoal; **LT**: Lithics; **HB**: Heated Bones; **BA**: Bones (all); **CP**: Coprolites; **SRF**: Slope Reworking Features; **BTF**: Bioturbation Features; **FMN**: Fe-Mn Nodules; **FL**: Fe-rich micro-lenses.

PF	TS	LY	PHC	CA	CH	LT	HB	BA	CP	SRF	BTF	FMN	FL
1	P1_1	GL1	–	*	*	–	**	**	**	**	*	**	–
1	P1_2A	GL2	–	*	–	–	***	**	*	**	*	**	–
1	P1_2B	GL3	–	*	*	*	**	**	*	**	*	*	–
1	P1_3A	GL3	–	**	–	–	**	*	*	**	*	*	–
1	P1_3B	GL4	–	**	–	–	*	*	**	**	**	***	**
1	P1_3C	GL4	*	*	–	–	**	*	*	***	*	***	**
1	P1_6A	GL4	*	***	*	–	*	*	***	*	***	*	–
1	P1_6B	GL4	*	***	–	–	–	*	***	***	**	**	*
1	P1_6C	GL4	–	***	–	–	*	*	***	**	**	*	–
1	P1_4A	GL5	–	*	–	–	*	*	*	**	–	**	–
1	P1_4B	GL5	–	*	–	–	–	–	*	**	–	**	–
1	P1_5	GL7	–	*	*	–	*	*	**	**	**	*	–
2	P2_1A	GL1D	–	**	*	–	***	**	*	***	–	**	–
2	P2_1B	GL1D	–	**	*	–	**	**	*	***	–	*	–
2	P2_2A	GL2	–	*	–	–	**	**	**	**	*	**	–
2	P2_2B	GL2	–	**	*	–	–	**	**	**	**	**	–
2	P2_2C	GL2	–	*	*	–	*	*	**	**	*	**	–
2	P2_3A	GL4	–	–	–	–	*	*	*	*	**	*	–
2	P2_3B	GL4	–	–	–	–	*	*	*	–	**	*	–
2	P2_5A	GL6	–	–	–	–	*	*	*	–	**	**	–
2	P2_5B	GL6	–	–	–	–	–	*	*	–	*	**	–
2	P2_4A	GL7	–	–	–	–	**	**	*	–	**	***	–
2	P2_4B	GL7	*	–	–	–	*	**	**	–	**	***	–
2	P2_6	GL7	–	–	–	–	–	***	*	–	**	***	–

layer resembles the reworked sediment aggregates found in the underlying layers, rich in Fe and characterized by aluminosilicate clays with a speckled b-fabric.

GL4B is separated from the underlying GL4A by a sharp erosional contact. Its composition is similar to GLs 5 and 7, with abundant rotational features indicative of reworking (Fig. 4d–e). Additionally, it is cemented with calcium carbonate and displays a calcitic crystallitic b-fabric and a higher concentration of carnivore coprolites. Crystallized rhizoliths were observed at the erosional boundary, suggesting a more stable period within the cave (Fig. 4d; SM8). Additionally, fresh rootlets observed in some thin sections are interpreted as modern intrusions from surface vegetation, penetrating the cave through existing fissures and joints in the karstic ceiling (SM8). Moreover, in this microlayer, we identified phosphatized reaction rims around and detached from limestone fragments (Fig. 5a–c), reflecting higher rates of coprolites and possible bat guano accumulation followed by sediment reworking (Karkanas et al., 2000; Shahack-Gross et al., 2004; Varis et al., 2022; Weiner et al., 1993).

GL4C shares similarities with GL4B but lacks cementation. It contains high amounts of coprolites and some digested bones. It is a reworked sediment, displaying a granular and open microstructure (Fig. 4g–h). The rotational features suggest that it was likely deposited by debris flows.

GL3 is a matrix-supported layer dominated by silt (46.2 %) and gravel (31.3 %) of quartz and limestone grains. As GLs 5 to 7, this layer displays rotational and deformation features typical of colluvial sediments, such as rounded aggregates with bones and coprolites. Furthermore, we identified rounded aggregates with a different sedimentary matrix compared to the surrounding deposit (Fig. 4i–j). Compared to lower layers, GL3 exhibits an increase in limestone fragments, which suggests more intensive breakage of the cave's ceiling and walls. Our excavation of this layer yielded a high concentration of bones and stone tools. Supporting these findings, our micromorphological analysis revealed fragments of lithic debitage exclusively in this layer (Angelucci, 2017). The micromorphological point-counting indicated a low frequency of carnivore coprolites (4.5 %).

GL2 is a matrix-supported sediment, rich in silt (61.1 %) and gravel (33.2 %) of quartz and limestone. The arrangement and accommodation of the sedimentary components are quite similar to GL3, displaying galaxy features, rounded aggregates, Fe- Mn nodules, and granostriated b-fabric (Fig. 4k). Furthermore, in this layer we found coarser grains than in GL3. This layer shows bones and stone tools, as well as carnivore coprolites (1 % based on counting in thin section), and as in GL4, in this layer we found phosphatic reaction rims around limestone fragments (Fig. 5d–h).

GL1 is the most superficial layer exposed in P1. It is a matrix-supported sediment with the highest concentration of silt (75.7 %) in the sequence, as well as the lowest percentage of quartz and limestone gravel (13 %). This layer is very similar to GL2, though displaying an increase in the number of limestone fragments. It shows an open microstructure and abundant sediment aggregates and granules, which contain most of the bones and coprolites (5 % based on counting in thin section). As displayed in SM8, micromorphological analysis revealed features consistent with deformation by slope processes, including galaxy or turbate structures and arcuate alignment of quartz and limestone grains (Phillips, 2006). These features were not visible macroscopically during excavation, likely due to the limited are exposed during our fieldwork. Above this layer, we identified a large limestone block, likely resulting from a partial roof collapse, which limited further sedimentation in this area of the cave.

The μ-XRF elemental quantification indicates that GL1 exhibits high concentration of Ca (32.8 %), Si (31.2 %), P (8 %), Al (7.5 %), and Fe (6 %). These elements are related to the clays that compose the sediments in the whole sequence, as well as the limestone bedrock and the carnivore/bat-derived phosphates. By fluorescence microscopy, we also identified heated bones (Fig. 4l–m) mixed with fresh bones.

4.1.4. Spearman correlation results – profile P1

In P1, the correlation between coprolites and lithics was positive ($\rho = 0.61$), but not statistically significant ($p \approx 0.15$). The correlation between coprolites and faunal remains was also positive but weak ($\rho = 0.21$, $p \approx 0.63$). No statistically significant relationships were observed in this profile.

4.1.5. Geochemical results

In Profile 1 (P1), silicon dioxide (SiO_2) concentrations increase with depth, from 40.27 % in the uppermost layer (GL1) to 59.94 % in the basal layer (GL7). Aluminum oxide (Al_2O_3) follows a similar trend,

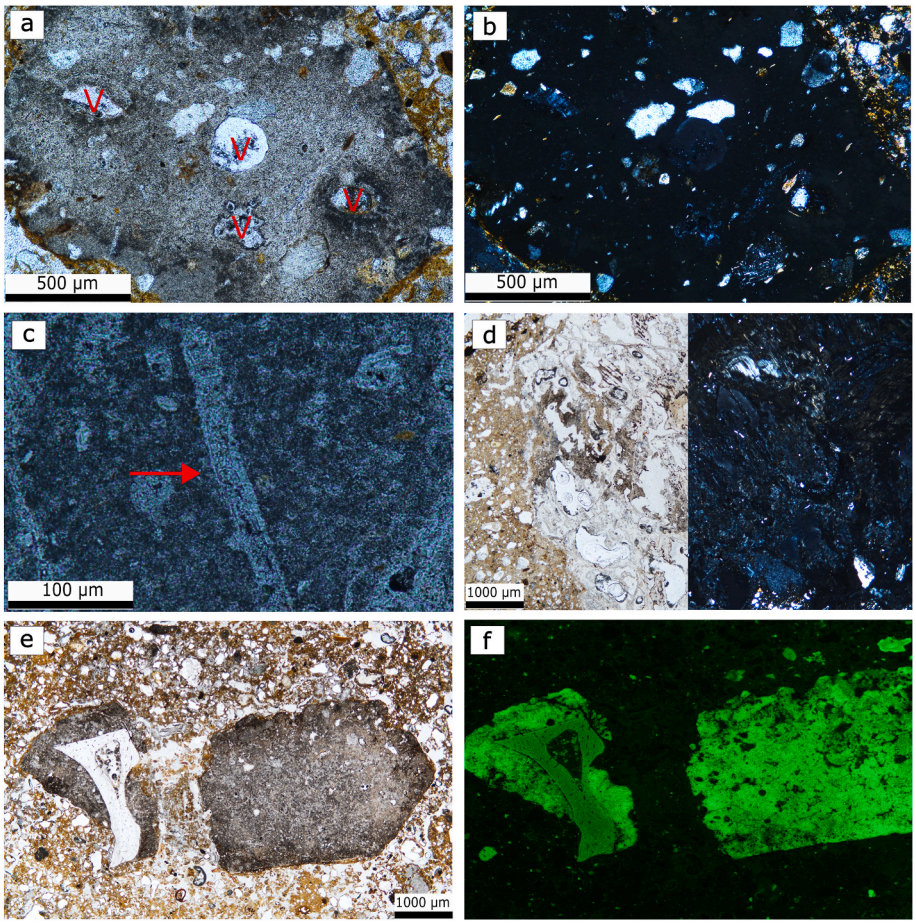

Fig. 3. Carnivore input at Escoural. a) Photomicrograph in PPL from thin section P1-6A (GL4) depicting a carnivore coprolite, with a dense greyish cortex with a phosphatic matrix, digestive gas bubbles or voids (V), and dark brownish punctuations linked to organic matter. **b)** Same as (a) but in XPL. displaying admixtures with fine sand-sized quartz. Note the isotropic nature of the phosphatic matrix in XPL. **c)** Photomicrograph in PPL from thin section P1-6A (GL4) exhibiting calcitic pseudomorphs related to hair fibers (red arrow) (Sanz et al., 2016). **d)** Photomicrograph in PPL and XPL from thin section P2-4A (GL7) depicting a digested bone, highly degraded. **e)** Photomicrograph in PPL from thin section P1-3B (GL4) depicting two carnivore coprolites, note a bone fragment inside the left one, the massive internal microstructure, and the darker brown rim on the edges. **f)** Detail from (e) under Blue Fluorescence. Note the high fluorescence of both the bone and the coprolites. (For interpretation of the references to color in this figure legend, the reader is referred to the Web version of this article.)

ranging from 8.11 % in GL1 to 11.67 % in GL7. Total iron oxide (Fe_2O_3(T)) also increases downward, from 5.79 % in GL1 to a maximum of 7.34 % in GL7 (Fig. 6).

Calcium oxide (CaO) shows the opposite pattern, with values decreasing from 17.80 % in GL1 to 3.64 % in GL6. Total inorganic carbon (TIC) increases from 0.18 % in GL7 to 1.53 % in GL2, then decreases slightly to 1.21 % in GL1. Total organic carbon (TOC) is highest in GL1 (0.75 %) and lowest in GL3 (0.12 %).

Phosphorus pentoxide (P_2O_5) concentrations reach their maximum in GL4, with values of 7.75 % and 6.76 % (samples 552 and 553, respectively). Percentage of Loss on ignition (LOI) is also relatively high in GL4 (10.40 %–12.09 %), with the highest value in the profile observed in GL3 at 16.16 %. Total carbon (TC) ranges from 0.50 % in GL5 to 1.95 % in GL1. The carbon-to-nitrogen (C/N) ratio increases upward, from 0.84 in GL3 to 4.92 in GL1.

4.2. Profile 2 (today outside the cave)

4.2.1. 2020's excavation results

In P2, we distinguished 7 sublayers within GL1 (A to G) (Table 4) Our GLs largely correspond to those previously identified by Otte and Silva (1996). The most notable exception is their layer 2, corresponding to our GLs 1C to 1D. Our work at P2 involved cleaning the sediment profile and the excavation of a 50 × 50 cm and 30 cm deep pit, unearthing GL7. Therefore, the materials we documented in P2 consist of only 26 Mousterian stone tools and 60 faunal bones, both counts correspond to total station points, with the majority of material concentrated in Layer 4. This layer accounted for 65 % of the bones (n = 39) and 65 % of the lithics (n = 26). Previous excavations of GL4 unearthed a homogeneous quartz lithic assemblage, which was assigned to the Mousterian (Otte and Silva, 1996). Layer 2 contained a smaller quantity of material, with 5 bones (8.3 %) and 1 lithic artifact (2.5 %). No archaeological material was recovered from Layers 1D, 6, or 7. Additionally, 16 bones (26.7 %) and 13 lithics (32.5 %) had no clear stratigraphic attribution. These unassigned materials were recovered during the removal of backfill sediment located directly in front of the profile. As this sediment likely originated from previous excavations, the materials are considered out of stratigraphic context.

4.2.2. Micromorphology and µ-XRF

GL7 is at the base of the exposed sequence. This layer was not unearthed in previous excavations. Our excavation stopped before reaching the bedrock due to safety concerns. However, an ongoing geophysical study suggests that the sequence extends deeper, and future excavations aim to uncover deposits underlying GL7.

GL7 is a matrix-supported sediment rich in gravel (57.3 %) and silt (34.1 %) of quartz and few limestone grains. Some limestones show dogtooth features and phosphatic rims similar to P1 (Fig. 5i–k).

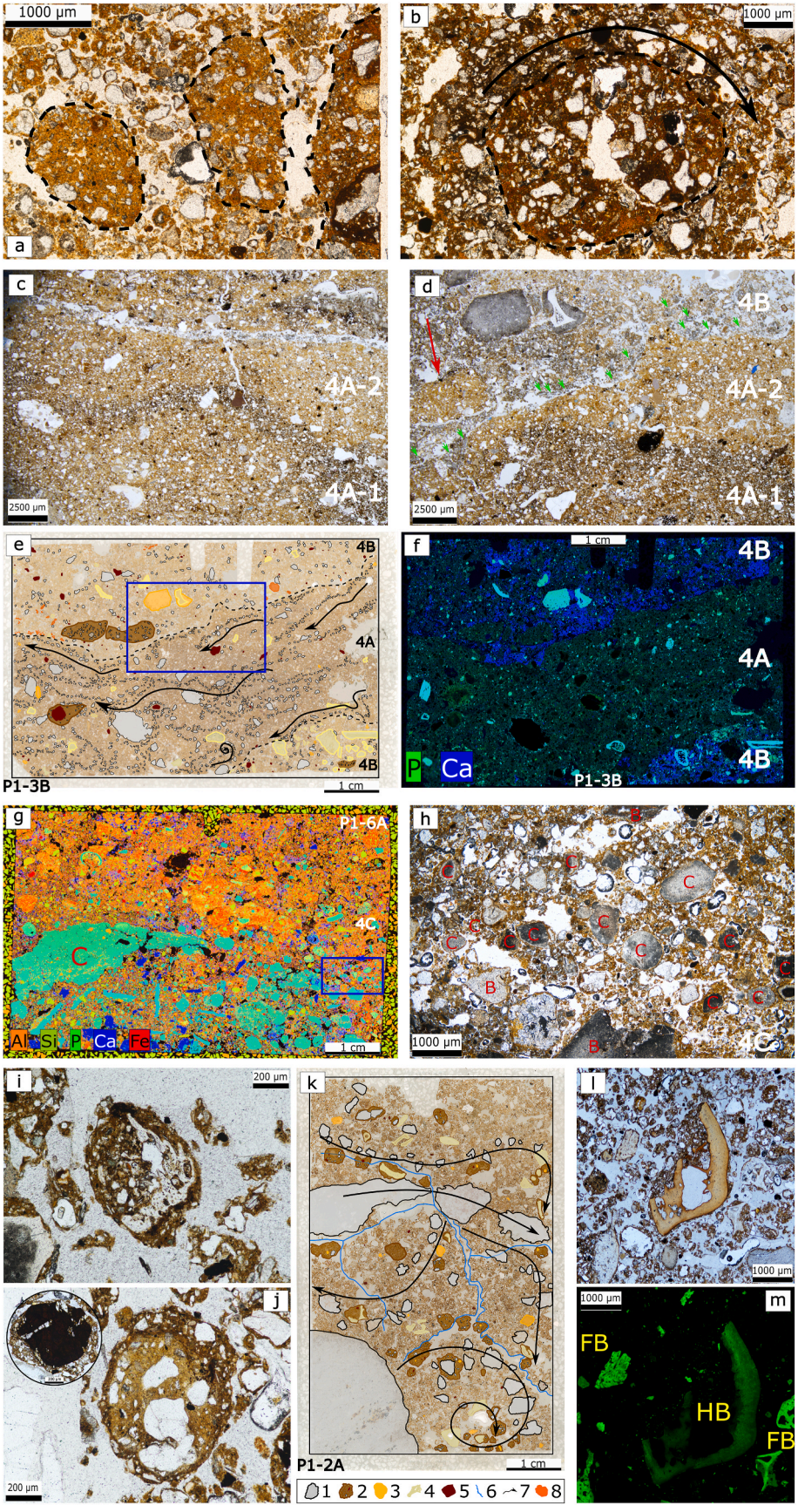

(caption on next page)

Fig. 4. Representative features from P1. Additional and unannotated photomicrographs and scans of the thin sections presented here are available in Supplementary Material SM8. **a)** Photomicrograph in PPL from thin section P1-5 (GL7) depicting rounded aggregates embedded in an open microstructure ground mass. **b).** Photomicrograph in PPL from thin section P1-4B (GL5) displaying a rounded sediment aggregate with rotational features from GL5. Note the circular alignment of silts and sands of quartz surrounding the aggregate. **c)** Photomicrograph in PPL from thin section P1-3C displaying microlenses 4A-1 rich in Fe, and discrete sorting of sand-sized quartz, and 4A-2 with a yellowish micromass. **d)** Photomicrograph in PPL from thin section P1-3B, detail of blue square in (e). Note the microlenses, the rounded sediment aggregate (red arrow) linked to reworking, as well as the calcified rhizoliths (green arrows) along the erosional contact between 4A and 4B. **e)** Scan of thin section P1-3B from GL4, illustrating processes related to colluviation within the cave. The central microlayer, 4A, exhibits phosphatization as demonstrated in (i) and shows grain size grading from fine to coarse particles, indicative of sheetwash. Microlayer 4B is rich in coprolites and bones, and is calcified, as shown in (f). **f)** μ-XRF elemental mapping of (e), illustrating the distribution of calcium (Ca) and phosphorus (P) and revealing the phosphatized (4A) and calcified (4B) microlayers. **g)** μ-XRF elemental mapping of thin section P1-6A (GL4C) displaying a matrix-supported sediment dominated by aluminosilicate clays. Note the centimetric carnivore coprolite surrounded by small, rounded coprolites in light green. **h)** Photomicrograph in PPL, detail of blue square in (g), corresponding to microlayer 4C, depicting a high accumulation of rounded carnivore coprolites (C) in a reworked sediment mixed with bones (B) and aggregates. **i)** Photomicrograph in PPL from thin section P1-2B (GL3) depicting a rounded sediment aggregate comprising a bone fragment with rotational features indicating reworking. **j)** Photomicrographs in PPL from thin section P1-3A (GL3) displaying a rounded sediment aggregate with a matrix and coating of different coloration. This contrast suggests the aggregate may originate from a different depositional context and was later reworked and coated during slope processes. In detail, note an anorthic Fe nodule coated by silty clay sediment (scale: 200 μm). **k)** Scan of thin section from GL2 (P1-2A), illustrating various processes associated with colluviation within the cave, including 'galaxy' or turbate structures (Karkanas and Goldberg, 2018; Phillips, 2006). In the image we highlighted: **1**) coarse grains (quartz and limestone); **2**) sediment aggregates; **3**) coprolites; **4**) bones; **5**) Fe-Mn nodules; **6**) pores; **7**) transport direction; and **8**) roots. **l)** Photomicrograph in PPL from GL1 (thin section P1-1A) showing a heated bone in a groundmass predominantly composed of limestone, rounded aggregates, bones, and coprolites. **m)** Same as (l), illustrating the weak fluorescence of heated bones (HB) contrasted by the higher fluorescence of fresh bones (FB) (Lambrecht and Mallol, 2020). (For interpretation of the references to color in this figure legend, the reader is referred to the Web version of this article.)

Rotational features are rare, suggesting limited reworking. Midway through the layer, we observed a localized, centimeter-thick breccia lens during excavation. This breccia consists of medium-sized limestone gravel, calcite/dolomite sand, and scattered charcoal fragments concentrated in darker laminations. Although our micromorphological samples were not taken directly from the brecciated portion, thin section analysis revealed a high number of coprolites (27 % based on counting in thin section), phosphatic crusts and nodules, and millimetric to centimetric digested faunal bones. Furthermore, the μ-XRF elemental quantification shows that there are high Ca and P concentration within this layer, which is coherent with a cave environment with an important input of carnivores feces and urine, as well as bat guano (Fig. 7a–b) (Braillard et al., 2004; Mallol and Goldberg, 2017). Interestingly, we found limited human input consisting of combustion residues, such as charcoal and charred plant tissues (Fig. 7c).

GL6 is a matrix-supported sediment similar to GL7, rich in gravel (42.3 %), silt (32.6 %), and sand of quartz and quartzite. The c/f related distribution is close porphyric with complex packing voids. Thin section analysis revealed a sharp decrease in carnivore coprolites (9 % based on counting in thin section) and less intensive bone weathering. No stone tools or bones were recovered. This layer appears more reworked than GL7, primarily by bioturbation (Fig. 7dj).

GL4 is a matrix-supported sediment rich in sand (36.6 %) and silt (32.4 %) of quartz and quartzite. Compared to layers below, there is a decrease in grain size of the sedimentary components, but an increase in bioturbation due to roots and soil mesofauna. Thus, we identified an open microstructure with abundant rounded granules, rich in silt and sand of quartz. Porosity is dominated by chambers, channels, and planar voids (Fig. 7e). This layer shows increased carnivore and anthropogenic input, with high number of coprolites (14 % based on counting in thin section), bones, and stone tools.

GL2 is located atop a large limestone block. It is a matrix-supported sediment, rich in sand (37 %), gravel (33 %), and silt (28 %) of quartz and limestone**.** Carnivore activity appears high, with 41 % of coprolites observed in the profile (thin-section count), while human input seems low, with few stone tools recovered. However, since this data is based on profile cleaning rather than excavation, visibility biases may influence these proportions. Furthermore, we observed combustion residues, such as charcoals associated with heated bones. Additionally, we identified burnt organic matter coated with ashes, in the form of rhombic and micritic pseudomorphs of calcium oxalates (Fig. 7f) (Canti and Brochier, 2017; Mentzer, 2014).

Int the lower part of the layer most of the carnivore and anthropogenic remains we observed are embedded within centimetric sediment aggregates, some of which exhibit a different sedimentary matrix than the surrounding deposit (Fig. 7g–i). Limestone sand-sized grains are concentrated in the upper part of the layer, with rotational features such as coatings of dense silty-clays with granostriated b-fabric (Fig. 7j), which are related to slope processes previous to the rock fall events which are evident in the upper layers of the sequence.

Previous excavators argued that the deposits below GL1 formed as cave sediments (GLs 7 to 2), when this site area was roofed by the large limestone boulders that later collapsed on top of the sequence (Otte and Silva, 1996). The high frequency of carnivore coprolites we observed in GL 2 and its underlying layers supports this interpretation, linking these deposits to a deeper cave environment occasionally visited by carnivore and affected by slope reworking (Discamps et al., 2012; Stewart et al., 2021).

GL1D is located at the top of the sequence, below a large boulder of limestone, which is linked to rock fall events. It is a clast-supported sediment, rich in gravel, coarse sand and silt of limestone and quartz. Most of the quartz and limestone grains show rough angular to subangular edges. There are mixed calcitic crystallitic and speckled b-fabrics in the groundmass, and the fine fraction is crumbly and loose. In this layer we also identified calcium carbonate features, such as calcified rhizoliths, coatings, and infillings, the latter of which are related to the degradation of limestones. We did not recover bones or stone tools in this layer during the cleaning of the profile, but thin section analysis unveiled some coprolites (8,75 %), fresh and heated bones, and charcoals. Additionally, we identified abundant Fe-Mn nodules (Fig. 7k), bones coated with dense silty-clays and granostriated b-fabric (Fig. 7l), as well as abundant rotational features such as galaxy and arcuate structures (Fig. 7m) (Karkanas and Goldberg, 2018; Phillips, 2006).

This layer provides valuable insights into the characterization of slope processes in thin section analysis. As illustrated in Fig. 8, various stages in the formation of rounded sediment aggregates and turbate structures resembling galaxy patterns were identified. The process begins with loose grains that are minimally coated by silty clay sediments (Fig. 8a), progresses to the initial aggregation of diverse sedimentary components such as bones, coprolites, Fe-Mn nodules, quartz, limestone, metamorphic grains, and clays (Fig. 8b), and culminates in fully rounded sediment aggregates (Fig. 8c). Some of these aggregates display circular and arcuate grain alignments, indicating the direction of the slope (Fig. 8d).

Our data are coherent with the previous investigations from the 1960s and 1990s, where the excavators described this layer as a heavily reworked mix of archaeological materials from different periods spanning from Chalcolithic to Neolithic (Otte and Silva, 1996).

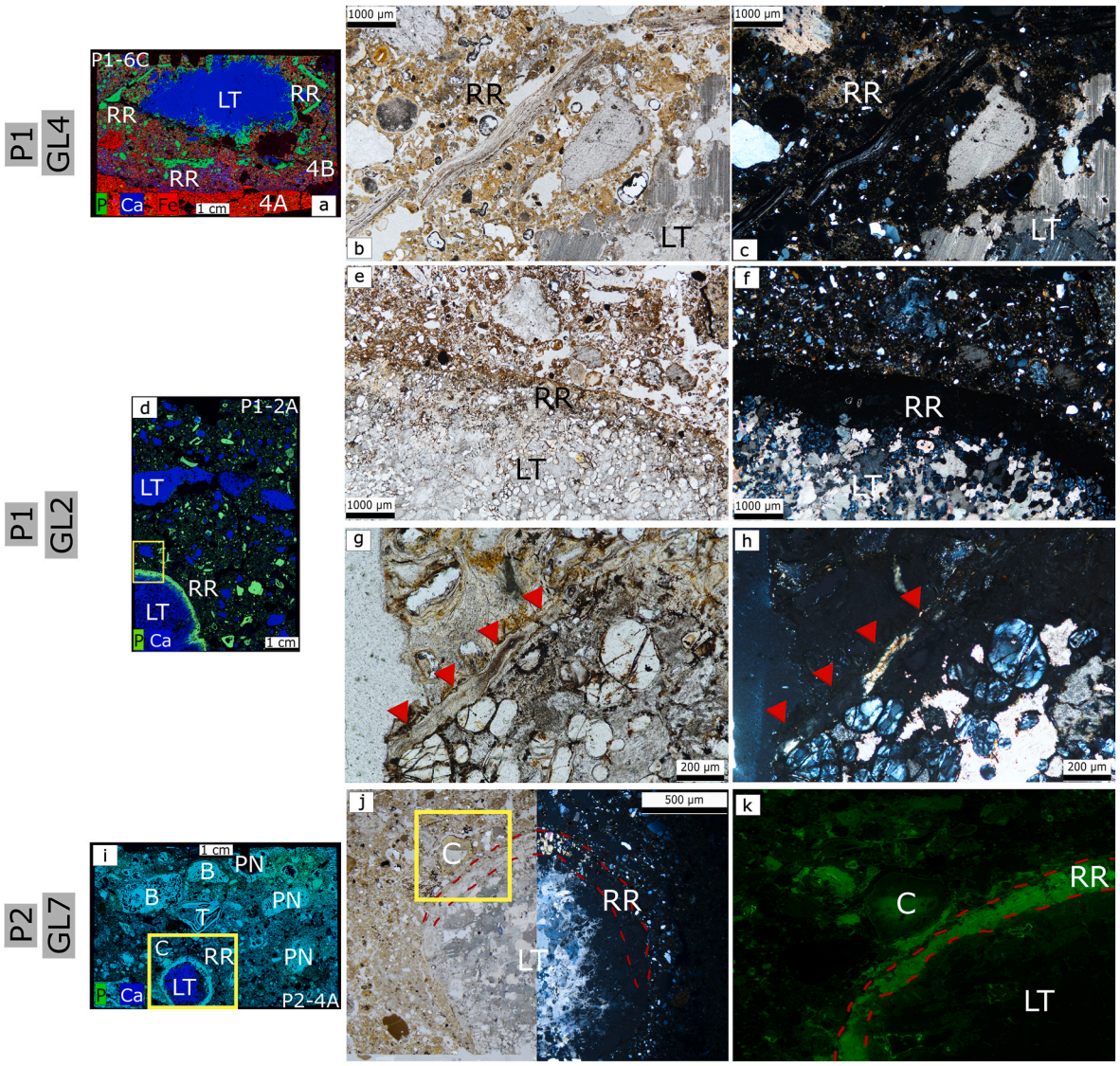

Fig. 5. Interactions between calcium carbonate and phosphates. a) µ-XRF elemental mapping of thin section from P1-6C (GL4), depicting a big limestone fragment (LT) and the detached reaction rims around (RR). **b)** Photomicrograph in PPL from thin section P1-6C depicting the reaction rim detached from limestone and broken, in GL4B. **c)** Same as **(b)** but in XPL. **d)** µ-XRF elemental mapping of thin section from P1-2A (GL2). Note the centimetric limestone fragments (LT) and the reaction rim (RR) coating the lowermost fragment sampled in the block. **e)** Photomicrograph in PPL from P1-2A depicting the apatite reaction rim (RR) and the incipient dissolution of limestone (LT). **f)** Same as **(e)** but in XPL. Note the isotropic nature of apatite. **g and h)** Photomicrographs in PPL and XPL depicting another section of the same apatite rim in the thin section P1-2A but exhibiting a likely laminated feature. **i)** µ-XRF elemental mapping of thin section from P2-4A (GL7), displaying a rounded limestone fragment (LT) coated with an apatite reaction rim (RR) in a ground mass comprising coprolites (C), phosphatic nodules (PN), bones (B) and teeth (T). **j)** Photomicrograph in PPL and XPL from thin section P2-4A showing the degradation process of limestone (LT) with the reaction rim (red dashed lines). **k)** Blue Fluorescence. Detail of the phosphatic rim around a limestone (LT) from the yellow square in **(j)**. Note the high fluorescence of the apatite that composes the rim as well as the fluorescence of the coprolite (C) above it. (For interpretation of the references to color in this figure legend, the reader is referred to the Web version of this article.)

4.2.3. *Spearman correlation results – profile P2*

In P2, the test revealed a strong negative correlation between coprolite relative abundance and lithic artifact proportions ($\rho = -0.90$), which was statistically significant ($p \approx 0.037$). Correlation between coprolites and faunal remains was negative but not statistically significant ($\rho = -0.40$, $p \approx 0.50$).

4.2.4. *Geochemical results*

In P2, the upper part of the sequence (GL2 to GL4; samples 204–207) shows relatively consistent elemental concentrations (Fig. 9). Silicon dioxide (SiO_2) ranges from 44.02 % to 49.67 %, aluminum oxide (Al_2O_3) from 8.61 % to 10.53 %, and total iron oxide (Fe_2O_3(T)) from 5.42 % to 6.67 %. Calcium oxide (CaO) values vary moderately within this interval, between 9.50 % and 14.84 %. Loss on ignition (LOI) ranges from 10.63 % to 13.95 %, while phosphorus pentoxide (P_2O_5) is highest in GL2 (10.92 %) and decreases through GL4 (down to 4.25 %).

Sample 208 (GL6) exhibits the most distinct geochemical values within the profile. It records the lowest concentrations of SiO_2 (34.20 %), Al_2O_3 (7.27 %), and Fe_2O_3(T) (5.20 %), and the highest values of CaO (23.63 %) and LOI (18.95 %). This sample also has the highest total inorganic carbon (TIC) at 2.19 %, and the lowest total organic carbon (TOC) at 0.18 %, resulting in the lowest carbon-to-nitrogen ratio (C/N) in the profile at 1.15.

Sample 209 (GL7) shows elevated P_2O_5 (6.31 %), the highest in the profile after GL2. Major oxides are moderate in concentration: SiO_2 at 48.21 %, Al_2O_3 at 9.37 %, Fe_2O_3(T) at 6.35 %, and CaO at 12.01 %. LOI

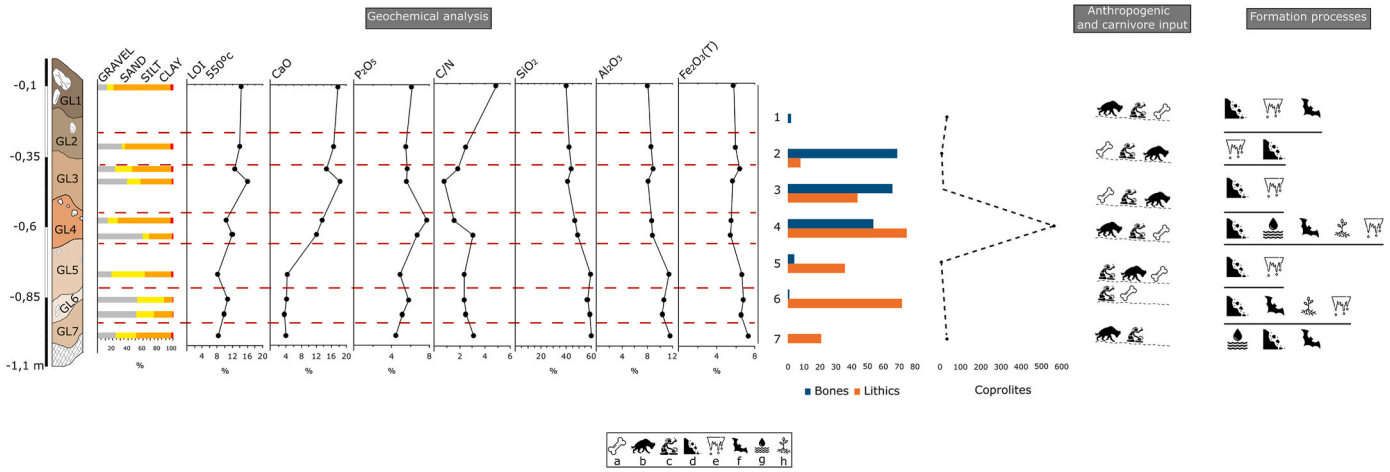

Fig. 6. Schematic description of the stratigraphy, grain size, key geochemical analysis, anthropogenic and carnivore input, and site formation processes in P1. The quantification of bones and lithics comes from data recovered in our team's archaeological campaign. The coprolites were point-counted in the micromorphology thin sections. °**a)** Faunal bones (fresh and heated); **b)** Carnivore input (coprolites); **c)** Stone tools; **d)** Colluviation; **e)** Calcium carbonate precipitation; **f)** Guano; **g)** Slope-wash; **h)** Bioturbation.

Table 4
Summary of field description of the layers and associated micromorphology thin sections of P2.

Layer	Thin section	Field description
GL1A	N/A	Layer localized in the west profile of the 1990s excavation. Loose brown sediment interspersed with limestone and marble fragments, ranging in size up to 40–50 cm. The archaeological material within this layer—including pottery shards, lithic artifacts, faunal remains, and human bones—is scattered and originates from multiple periods. The presence of fragmented and dismantled breccia highlights significant disturbances at this level, likely associated with embankments created during previous excavations.
GL1B	N/A	Layer localized in the west profile of the 1990s excavation. Uniform black humus layer. It contains some reworked archaeological material and, based on its position at the summit and evidence of landslides, may predate the investigations conducted by Dos Santos (1964).
GL1C	N/A	Frequent gravels to boulders of limestone and dolomite in silt, with little clay and sand (up to coarse sand). Weakly bedded.
GL1D	P2_1A, 1B	Similar to GL1C, but with less gravel (especially less coarse gravel and boulders). The sediment is more compact.
GL1E	N/A	Coarser gravel (limestone and dolomite) than GL1D. The fine fraction is similar to the above. Sediment is more compact than the above layers.
GL1F	N/A	Similar to GL1E. The gravel is imbricated and slopes towards E, NE, NW, and W with angles between 5 and 30°.
GL1G	N/A	Bioturbated layer, with granular, reworked loose sediment related to a burrow.
GL2	P2_2A, 2B, 2C	Boulders and rare coarse and medium gravel of limestone (at the bottom of the unit) in a silty clay sediment. In the middle of the layer, we identified a localized subangular coarse gravel/small boulder of breccia. Rare fine gravel of limestone, common medium to coarse sand of white and yellow calcite.
GL3	N/A	Silt, loose, rich in roots. Rare medium gravel of limestone.
GL4	P2_3A, 3B	Fine fraction composed of silty sand.
GL5	N/A	Breccia. Medium sand to fine gravel of calcite/dolomite, charcoal, and faunal remains.
GL6	P2_5A, 5B	Sandy silt with numerous roots and fine to medium gravel fragments of limestone and breccia.
GL7	P2_4A, 4B, 6	Well-sorted sandy silt with little clay. Sand is medium to coarse. In the bottom, this layer appears more platy than in the above sediments. In the middle, we identified macroscopically a localized centimetric layer of breccia, similar to breccias above. In this microlayer there are medium gravel of limestone, fine to coarse sand of calcite/dolomite, up to coarse sand grains of charcoals.

is also relatively high at 11.45 %. TIC and TOC values are 0.65 % and 0.45 %, respectively, with a C/N ratio of 2.95.

5. Discussion

5.1. Sources of sediments and archaeological materials

Our results, combined with 1990s excavation data, allow us to reconstruct depositional and post-depositional processes at P1 and P2. Both sequences show layers composed of mixed autogenic and allogenic components (Stratford, 2024). Autogenic materials include calcium carbonate precipitates, limestone and dolomite fragments from cave walls/roof, and metamorphic rocks like hornfels and gneiss. Neoformed apatite, likely from carnivore excrements, urine, decayed carcasses, and bat guano, occurs in both profiles (Fig. 3). This is supported by low C/N ratios (<10), indicating protein-rich sources (Benedetti et al., 2019; Finlay and Kendall, 2007; Forbes et al., 2007; Gleixner, 2013; Jover et al., 2014; Meyers, 1997; Peterson and Fry, 1987). Though phosphate formation usually occurs under mildly acidic conditions (pH 6–7) (Barbieri, 2019; Friesem et al., 2019; Friesem et al., 2022, p. 222; Goldberg and Sherwood, 2006; Karkanas et al., 2002; Mallol and Goldberg, 2017; Shahack-Gross et al., 2004), our geochemical data show a basic to alkaline pH (7.6–8.5), suggesting secondary carbonate precipitation after phosphate accumulation.

Allogenic indicators—including Fe-Mn nodules (Figs. 4 and 7) (Vepraskas et al., 2018), aluminosilicate clays, and angular quartz grains—point to an external origin. While no direct comparative samples were taken, micromorphology and elevated SiO_2, Al_2O_3, and Fe_2O_3(T) support derivation from weathered soils (Helland et al., 1997; Krinsley and Doornkamp, 1974). The quartz grains particular exhibit angular morphologies consistent with short-distance, gravity-driven colluvial transport. Crucially, Escoural cave's dolomitic bedrock lacks quartz, confirming an allochthonous source. A potential source is the nearby Complexo Vulcano-Sedimentar de Moura–Santo Aleixo, specifically the Xistos de Moura unit, which outcrops approximately 600 m west (LNEG, 2024). This Ordovician–Silurian complex includes basic volcanic and metamorphosed sedimentary rocks likely containing quartz and feldspar. Erosion of these materials likely contributed to soil formation on the slopes near the cave. These soils, enriched in quartz and aluminosilicates, may have been transported into the karst system via natural fissures and entrances during the Pleistocene, when the cave likely functioned as a porous structure. This colluvial process explains the sediment mixing in P1 and upper P2.

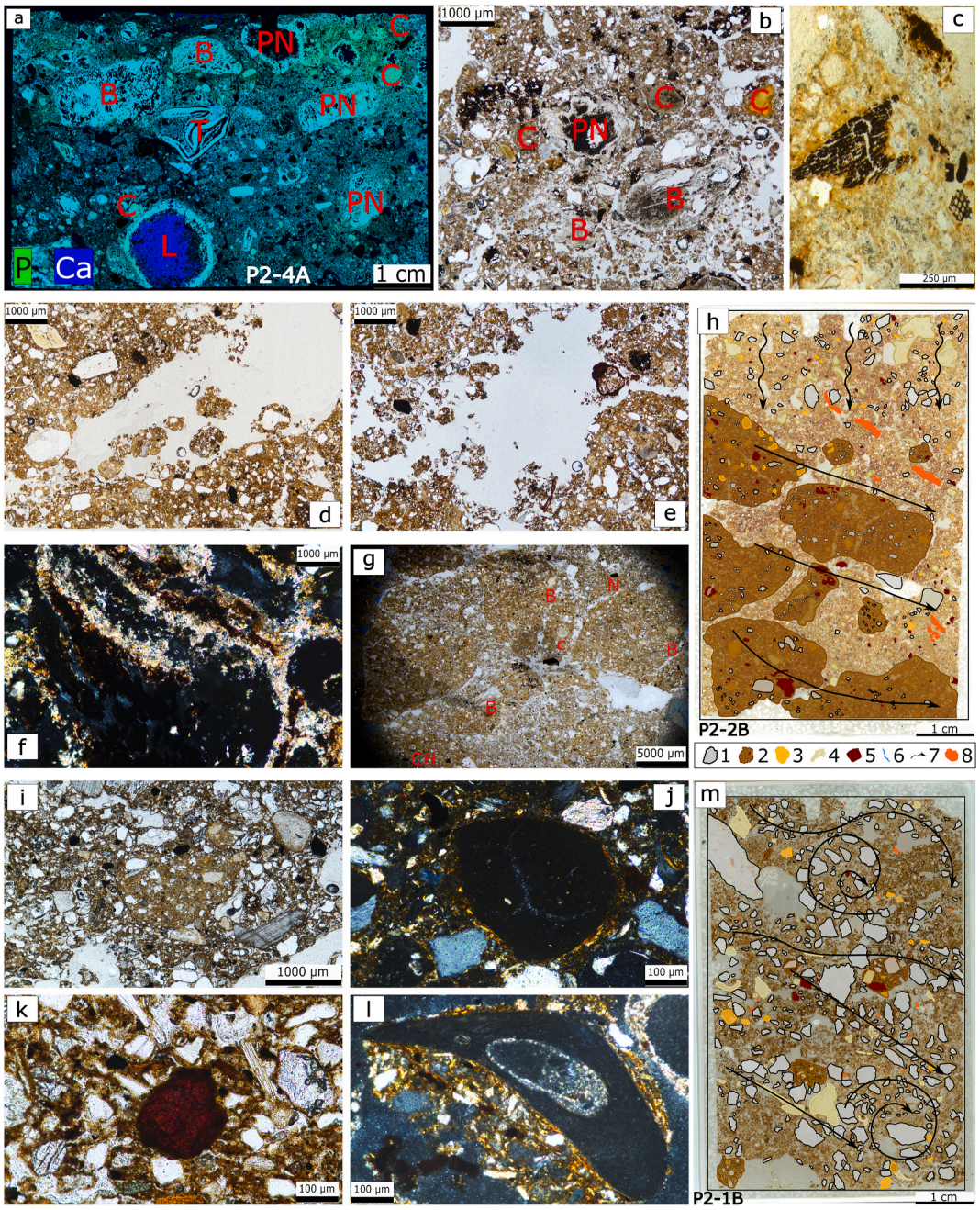

Fig. 7. Representative features from P2. Additional and unannotated photomicrographs and scans of the thin sections presented here are available in Supplementary Material SM8. **a)** µ-XRF elemental mapping of thin section P2-4A (GL7). Note the high amount of phosphorus, related to coprolites (C), bones (B), teeth (T), and phosphatic nodules (PN), particularly of a carnivore den. In the bottom, a limestone fragment with a reaction rim due to the incipient process of phosphatization. **b)** Photomicrograph in PPL from thin section P2-6 (GL7) depicting mixed anthropogenic and carnivore input with fresh and heated bones (B), coprolites (C), digested bones, and charred organics. **c)** Photomicrograph in PPL-OIL from thin section P2-4A (GL7) depicting charcoal and charred plant tissues. **d)** Photomicrograph in PPL from thin section P2-5A (GL6) depicting a bio-channel infilled with rounded sediment aggregates linked to bioturbation. **e)** Photomicrograph in PPL from thin section P2-3A (GL4) depicting bioporosity due to root and soil fauna activity in the sediment. Note the granular microstructure close to the walls of the channel, as well as abundant mite excrements and root relicts. **f)** Photomicrograph in XPL from thin section P2-2C (GL2) depicting charred organic matter with a coating of ashes in the form of rhombic and micritic pseudomorphs of calcium oxalates (Canti and Brochier, 2017; Mentzer, 2014). **g)** Photomicrograph in PPL from thin section P2-2B (GL2) depicting the middle part of (f), showing the sediment aggregates comprising bones (B), coprolites (C), charcoal (CH) and Fe-Mn nodules. **h)** Scan of thin section P2-2B (GL2), illustrating various processes associated with the transition between the first phase of colluviation in the lower part, and remnants of the rock fall event in the upper part of the section. The lower part displays some centimetric rounded sediment aggregates, containing high amounts of bones and coprolites. The image highlights: **1**) coarse grains (quartz and limestone); **2**) sediment aggregates; **3**) coprolites; **4**) bones; **5**) Fe-Mn nodules; **6**) porosity; **7**) direction of transport; and **8**) roots. **i)** Photomicrograph in PPL from thin section P2-2A (GL2), showing a sediment aggregate with a matrix clearly distinct from the surrounding sediment, further supporting the presence of reworked materials with potentially different provenance. **j)** Photomicrograph in XPL from thin section P2-2B (GL2) depicting a carnivore coprolite coated by granostriated b-fabric clays. **k)** Anorthic Fe nodule. Photomicrograph in PPL from thin section P2-1A (GL1D). **l)** Same feature as (j), but a bone fragment from thin section P2-1A (GL1D). **m)** Scan of thin section P2-1B (GL1D), illustrating various processes associated with colluviation within the cave.

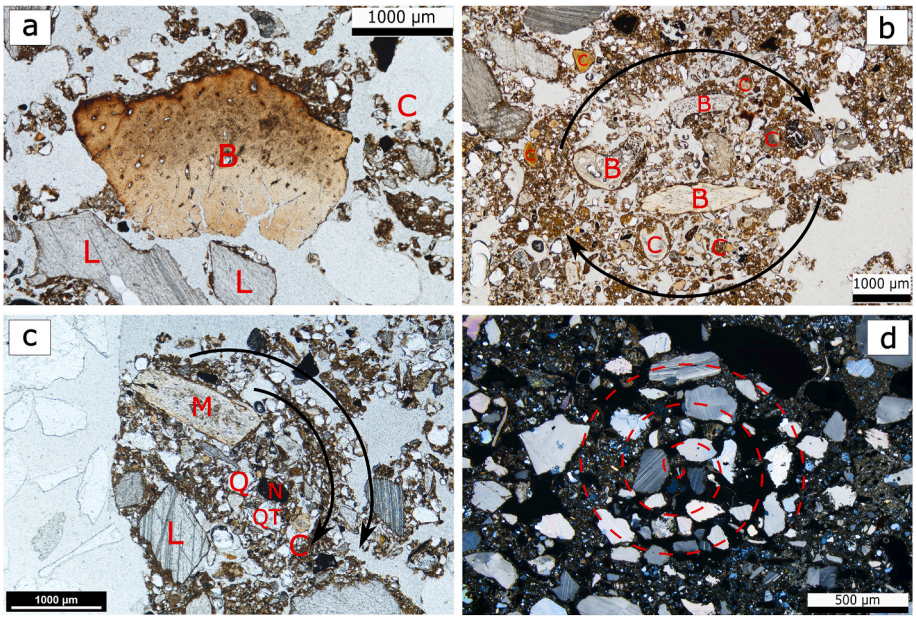

Fig. 8. Potential stages in the formation of sediment aggregates during debris flow colluviation. Unannotated versions of the photomicrographs are available in Supplementary Material SM8. **a)** Photomicrograph in PPL from thin section P2-1A (GL1D), showing the initial stage of a debris flow. Most coarse components such as bones and limestone fragments are partially coated with fine sediments, suggesting the early entrainment and transport of materials. **b)** Photomicrograph in PPL from the same thin section, representing an intermediate stage in the debris flow. Coarse and fine elements—including bones (B) and coprolites (C)—are arranged in rotational patterns, reflecting movement within the sediment mass. **c)** Photomicrograph in PPL from thin section P2-1B (GL1D), depicting an advanced stage of debris flow sedimentation. A rounded sediment aggregate is visible, exhibiting internal rotational structures (black arrows). The matrix is composed of speckled b-fabric clays, quartz (Q), quartzite (QT), metamorphic rock fragments (M), Fe-Mn nodules (N), and coprolites (C), indicating thorough mixing and redeposition. **d)** Photomicrograph in XPL from thin section P2-1A (GL1D), showing a sedimentary galaxy feature dominated by coarse limestone grains. Red dashed lines highlight rotational structures formed through slope reworking, distinct from the fine-dominated aggregates in (a–c). (For interpretation of the references to color in this figure legend, the reader is referred to the Web version of this article.)

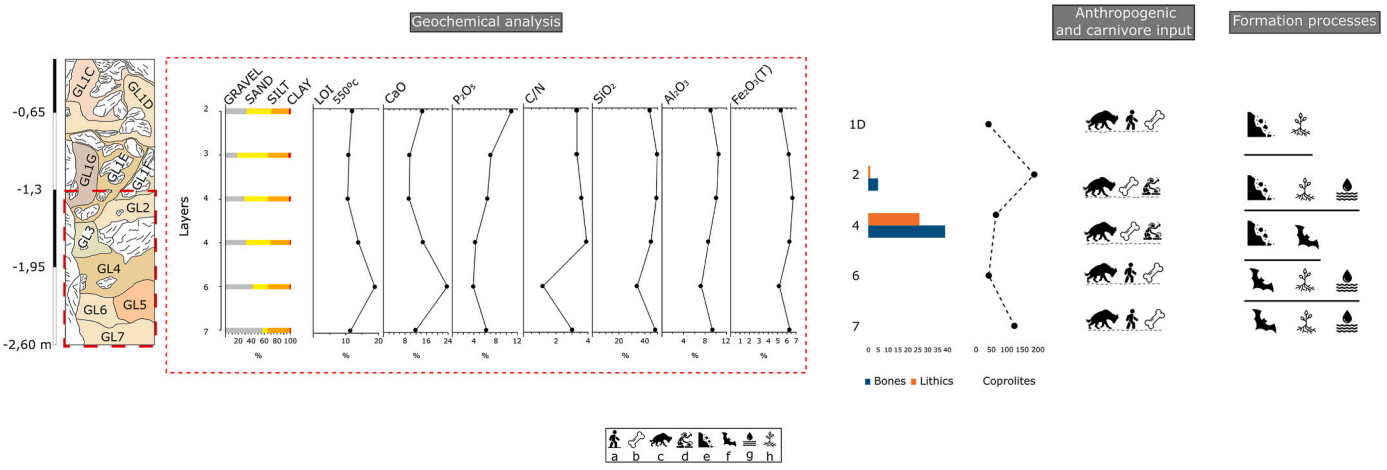

Fig. 9. Schematic description of the stratigraphy, grain size, key geochemical analysis, anthropogenic and carnivore input, and site formation processes in P2. The bones and lithic data come from our cleaning of the profile, and the coprolite data from the point-counting of features in micromorphological thin sections. Red dashed lines indicate the GLs covered by the grain size and geochemical analysis (GLs 2–7). **a)** Human input with no lithics; **b)** Faunal bones (fresh and heated); **c)** Carnivore input (coprolites); **d)** Stone tools; **e)** Colluviation; **f)** Guano; **g)** Water saturation; **h)** Bioturbation. (For interpretation of the references to color in this figure legend, the reader is referred to the Web version of this article.)

Further micromorphological evidence of downslope transport includes quartz and limestone grains, bones, coprolites, and sediment aggregates with different matrices, coated by silty clays with speckled b-fabric (Fig. 4; 7 and 8)—typical of colluviation. These likely entered the cave via natural fissures. While some features may reflect bioturbation, rotational structures and granostriated b-fabric point to dominant reworking by slope processes. The cave likely acted as a dynamic system, with gravity-driven processes introducing mixed sediments into P1 and upper P2. This also displaced archaeological materials like bones and coprolites, as evidenced by the aggregates observed in thin-section (Fig. 3d and e; 6c) (Bertran, 1993; Menzies and Zaniewski, 2003; Phillips, 2006). Lithics were not directly observed in these aggregates, but similar reworking may have affected their distribution.

Sediment and artifact movement in P1 appears tied to debris flows from Gallery 15 and areas by the Paleolithic entrance near P2 (Fig. 2a). Gallery 15 is 5 m north of P1 and 1.35 m higher than GL1. A former entrance, 7 m south of P1 and 2 m higher, is now filled with sediment. This layout suggests influx from near P2 is plausible, implying P1

archaeological materials were reworked from Gallery 15 and the P2 vicinity. The original geometry of this part of Escoural is obscured by sediment fill and earlier excavations, but micromorphological and chronological data, such as inverted radiocarbon dates support colluvial mixing. Further excavation in Gallery 15 and the cave exterior could help clarify this.

Geochemical trends complement these findings. In P1, decreasing SiO_2, Al_2O_3, and Fe_2O_3(T) values upward reflect reduced external input—possibly linked to source material erosion or sealing of upper entrances (Fig. 6). Simultaneously, increases in CaO and TIC suggest intensified carbonate precipitation. P_2O_5 peaks in GL4 and GL6 align with biological phosphate sources, while high LOI, TOC, and C/N ratios in GL4 point to organic-rich inputs from carnivore feces and bat guano. Micromorphology confirms the presence of phosphatized limestone and coprolite fragments. Uppermost P1 layers (GL3–GL1) show increased secondary carbonate, calcitic coatings, and rhizoliths, suggesting diagenesis linked to water percolation through carbonate-rich matrices.

Overall, the combined evidence indicates that carnivore and archaeological materials in P1 accumulated through repeated colluviation, interrupted by stable surface intervals, rather than a single event. Sharp stratigraphic boundaries in GL4 (Fig. 4c–h) mark environmental shifts, supported by microfacies changes. In GL4A, wetter conditions favored degradation of organic-origin inorganic materials (coprolites, guano, bones) and formation of Fe-rich micro-lenses by sheetwash erosion (Karkanas and Goldberg, 2018). In contrast, GL4B's drier settings enabled dry slope processes. Dense crystallized rhizolith formation at the GL4A/GL4B contact likely resulted from sedimentary breaks, supporting vegetation growth. This stable surface potentially attracted both Neanderthals and carnivores.

P2 is now an open-air sequence but was likely part of a roofed chamber during the Pleistocene (Otte and Silva, 1996). Excavations outside the cave revealed large limestone blocks from roof collapse and potential in situ cave wall segments. Micromorphology of GLs 7 to 2 shows phosphatized sediments with guano, coprolites, and anthropogenic inputs, indicating deposition in a roofed area (Fig. 7a–j).

Geochemical data further support this: GL7 shows the highest P_2O_5 (6.31 %), high percentage of LOI, and moderate oxide values. Micromorphology confirms intense carnivore activity (27 % coprolites), apatite formation, and limited charcoal—suggesting mostly carnivore use, punctuated by brief human presence. Macroscopically phosphate-rich breccia lenses in GL7, though not sampled for micromorphology, may reflect diagenetic processes driven by high biological phosphate input.

GL6 also stands out geochemically, showing high CaO and LOI values and reduced silicate content, consistent with breccia formation likely related to episodic hydrological shifts. However, absence of micromorphological data from this unit limits interpretation certainty.

GLs 7–4 in P2 exhibit micromorphological features consistent with primary deposition and minimal post-depositional disturbance, despite some bioturbation, distinguishing them from P1's mixed sediments. The absence of clear colluvial features suggests these units have not undergone significant mechanical reworking. Although Fe-Mn nodules, aluminosilicate clays, and quartz grains imply an allochthonous origin from weathered soils above the cave, these materials appear deposited through slow gravitational input or infiltration via ceiling fissures. While P2 is mid-slope today, during GLs 7–4 accumulation it was a roofed area limiting hilltop colluvial input. This makes P2 and surrounding areas a more reliable context for interpreting past human activity.

Upper P2 layers (GLs 2–1C) feature spheroidal peds, aggregates with distinct matrices, and Fe-Mn nodules, indicating reworking. Chaotic bone, coprolite, and sand-sized limestone distribution, with granostriated b-fabric, imply rotational deformation—possibly from partial roof collapse and colluviation (Friesem et al., 2022; Mücher et al., 2010; Stoops, 2020). This may have facilitated downslope transport of mixed sediments and archaeological materials of different ages. GLs 1A and 1B reflect a later, massive collapse that deeply buried P2 and disconnected it from the rest of the cave (Fig. 2a; 7k-m).

5.2. Neanderthal vs carnivores

Carnivores are often linked to animal and human bone accumulation in Paleolithic caves, especially at sites with limited human presence (Discamps et al., 2012; Horwitz and Smith, 1988; Sanz and Daura, 2018; Stewart et al., 2021). However, studies suggest hominids and carnivores typically did not cohabit (Linares-Matás and Yravedra, 2024; Picin et al., 2020). This pattern may be obscured in the archaeological record due to formation processes and low sedimentation rates, complicating distinguishing animal from human visits. Such challenges are evident at many Iberian Middle Paleolithic sites, including Gruta da Figueira Brava, Gruta do Caldeirão, Gruta Nova da Columbeira (Cardoso and Cascalheira, 2024), El Mirón (Marín-Arroyo et al., 2020), El Olivo (Mielgo et al., 2024), Teixoneres (Zilio et al., 2021), and Sopena (Pinto-Llona et al., 2024).

At Escoural, the distinction between alternating and potentially overlapping occupations is clearest when comparing P1 and P2. In P1, co-occurrence of lithics and coprolites within the same units might imply shared use by Neanderthals and carnivores. However, the lack of statistically significant correlations between these proxies (SM6), as well as micromorphological and geochemical evidence of sediment reworking, instead points to postdepositional mixing. Layers with highest carnivore input, (e.g., GL4), also show increased archaeological materials. While this could suggest fast alternation, it likely results from colluvial mixing, obscuring discrete occupation episodes and disrupts behavioral signals in the stratigraphy.

Nonetheless, GL5 yielded 17.5 % of total stone tools, suggesting a phase of more pronounced Neanderthal activity during reduced carnivore presence. This might reflect earlier Neanderthal use of southern cave chambers, including Gallery 15 and areas near P2.

In contrast, P2 presents a pattern more consistent with alternating use. An inverse distribution of lithic and coprolite concentrations across layers, with a statistically significant negative correlation, suggests Neanderthals and carnivores occupied this space at different times. Coprolite-rich layers (GL6, GL7) lack archaeological materials, while lithic-rich ones (e.g., GL4) show low carnivore presence. The relative stratigraphic integrity in lower P2 layers supports this. This area likely experienced episodic, discrete occupations by each group, supporting the interpretation that Neanderthals used this part of the cave intermittently—probably when the now-lost entrance was accessible—rather than for prolonged habitation.

6. Conclusions

Our stratigraphic, micromorphological, and geochemical data illustrate that the Escoural's cave system was significantly transformed by sedimentary and geochemical processes active during and after Neanderthal visits. P1, deeper inside the cave, retains reworked karstic sediments mixed with allogenic inputs, introduced and redistributed by colluviation and low-energy water flow. Inverted radiocarbon ages confirm archaeological finds in P1 resulted from reworking distinct assemblages. Lack of combustion features and limited fire residues in this light-deprived chamber further support the hypothesis that Neanderthals preferred to exploit areas of Escoural where fire use was not necessary. Given the cave geometry and sedimentary contacts, likely primary sources for P1 finds are nearby shallower chambers, such as Gallery 15, and areas around P2, now open-air due to collapses. Unlike P1′s Gallery 18, these offered more headroom and sunlight exposure, providing more comfortable settings for forager stays.

P2 is currently in a collapsed sector outside the present-day limits of the karst system. However, stratigraphic and micromorphological evidence from GLs 2 to 7 suggests that, compared to the actual setting, during the Middle Paleolithic, this area was part of a larger, shallow

chamber near the original cave entrance. While the precise Pleistocene entrance location remains uncertain, ongoing excavations indicate P2 lay within a broader accessible cavity later disrupted by roof collapse and modern quarrying. This space appears to have served as a shared occupation zone, used intermittently by both Neanderthals and carnivores.

We conclude Neanderthals primarily exploited Escoural areas closer to sunlight, contrasting Upper Paleolithic and later human groups that extensively utilized the deeper karst of the site (Araújo and Lejeune, 1995; Dos Santos, 1964; Lopes, 2013; Otte and Silva, 1996; Silva et al., 2023). These findings align with broader Eurasian patterns of Neanderthals predominantly occupying cave entrances rather than deep, enclosed spaces. Preference for well-lit areas suggests a site-use strategy focused on ease of access, visibility, and thermal comfort. Similar patterns are observed at other Iberian Middle Paleolithic sites (Angelucci et al., 2023; Arriolabengoa et al., 2018; Cardoso and Cascalheira, 2024; Lozano et al., 2024; Martín-Perea et al., 2023; Moclán et al., 2023; Picin et al., 2020; Zilhão et al., 2020).

The distribution of carnivore coprolites and Neanderthal cultural remains at Escoural suggests alternating rather than overlapping occupations. In P1, coprolite counts parallel archaeological find density, likely due to colluvial reworking mixing materials. In contrast, P2 shows an inverse relationship between carnivore and human activity, as evidenced by a significant negative correlation (Spearman's ρ), alongside micromorphological indicators of limited reworking in lower layers. Given this, it is unlikely Neanderthals and carnivores directly competed for space; instead, their stays appear to have alternated, as seen at other Iberian sites (Alcaraz-Castaño et al., 2017; Morales et al., 2019; Picin et al., 2020).

Our study reinforces previous interpretations about Neanderthal cave use and carnivore interaction, while paving the ground for further research at Escoural. Planned actions include excavations targeting undisturbed deposits (Gallery 15 and area outside the cave) geophysical surveys, refined absolute dating, and multi-proxy paleoenvironmental reconstructions. Combined with this study's results, these will further improve understanding of Escoural's role within the broader landscape of Neanderthal occupations in southwestern Iberia.

CRediT authorship contribution statement

Guillermo Alzate-Casallas: Conceptualization, Data curation, Formal analysis, Investigation, Methodology, Visualization, Software, Writing – original draft. **Ana I. Gomes:** Formal analysis, Methodology, Writing – original draft. **Nolan Ferar:** Methodology, Writing – original draft. **Sahra Talamo:** Writing – original draft. **Laura Tassoni:** Writing – original draft. **João Cascalheira:** Conceptualization, Funding acquisition, Project administration, Supervision, Validation, Resources, Writing – original draft, Writing – review & editing. **Alvise Barbieri:** Conceptualization, Project administration, Supervision, Validation, Resources, Writing – original draft, Writing – review & editing.

Declaration of competing interest

The authors declare that they have no known competing financial interests or personal relationships that could have appeared to influence the work reported in this paper.

Acknowledgments

We thank **Roxane Matias**, **Daniela Maio**, **Pedro Horta**, and **Milena Carvalho** for their help during the sample collection. We also thank the technician **Joana Rodrigues** for helping with the fluorescence microscopy at the Research Institute of the Algarve Biomedical Center in Faro, Portugal. Furthermore, we extend our appreciation to **Baltasar Deutor** from the Centro de Instrumentación Científico Técnica (CICT) of the University of Jaén (Spain), who helped with the μ-XRF analysis of the samples.

We also thank **Vera Aldeias, Carolina Mallol**, **Rosa María Poch,** and **Fabio Scarciglia** for their comments and help during the micromorphological analysis. As well as **Natalia Egüez** for her comments on the presentation of this work at the European Archaeologists Association meeting in August 2024 in Rome, Italy.

We thank **Ana Cristina Araújo** and **António Carlos Silva** for providing access to old reports, fieldnotes, and insights on some of the details about the late 1980's and early 1990's excavations.

The block samples were prepared at the Geoarchaeology Laboratory of the Interdisciplinary Centre for Archaeology and the Evolution of Human Behavior (ICArEHB) of the Universidade do Algarve (Portugal). The thin sections were produced at Spectrum Petrographic Inc. (USA).

This study was Funded by the European Union (ERC-CoG-2021, FINISTERRA, 101045506). Views and opinions expressed are however those of the author(s) only and do not necessarily reflect those of the European Union or the European Research Council Executive Agency. Neither the European Union nor the granting authority can be held responsible for them.

Sahra Talamo and **Laura Tassoni** have received funding from the European Research Council under the European Union's Horizon 2020 Research and Innovation Programme (grant agreement No. 803147 RESOLUTION, awarded to ST).

João Cascalheira, **Alvise Barbieri** and **Ana Gomes** are funded by the Fundação para a Ciência e a Tecnologia (respectively DL57/2016/CP1361/CT0026; 2002.08622.CEECIND; CEECINST/00146/2018/CP1493/CT0002).

Data availability

The data supporting this study's findings are available in the Open Science Framework (OSF) repository with DOI: 10.17605/OSF.IO/3A8DK. This repository serves as the research compendium for our quantitative and qualitative analyses, providing access to all datasets and supplementary materials associated with this publication. The dataset includes **.xlsm files** containing sediment grain size data and the GRADISTAT version 9.1 macro for analysis, **.xlsx files** with raw data from sediment elemental analysis, micro-XRF from thin sections, and radiocarbon dating, and two **.pdf files** with field descriptions of the stratigraphic sequences, and additional photomicrographs and scans of the thin section. These resources ensure transparency and facilitate the reproducibility of our findings.

References

Alcaraz-Castaño, M., Alcolea-González, J., Kehl, M., Albert, R.-M., Baena-Preysler, J., de Balbín-Behrmann, R., Weniger, G.-C., 2017. A context for the last Neandertals of interior Iberia: los Casares cave revisited. PLoS One 12 (7), e0180823. https://doi.org/10.1371/journal.pone.0180823.

Aldeias, V., Sandgathe, D., McPherron, S.J.P., Bruxelles, L., Turq, A., Goldberg, P., 2023. Site Formation Histories and Context of Human Occupations at the Paleolithic Site of La Ferrassie (Dordogne, France). Journal of Paleolithic Archaeology 6 (1), 30. https://doi.org/10.1007/s41982-023-00159-7.

Angelucci, D.E., 2017. Lithic artefacts. In: Archaeological Soil and Sediment Micromorphology, pp. 223–230. https://doi.org/10.1002/9781118941065.ch27.

Angelucci, D.E., Nabais, M., Zilhão, J., 2023. Formation processes, fire use, and patterns of human occupation across the Middle Palaeolithic (MIS 5a-5b) of Gruta da Oliveira (Almonda karst system, Torres Novas, Portugal). PLoS One 18 (10), e0292075. https://doi.org/10.1371/journal.pone.0292075.

Angelucci, D.E., Zilhão, J., 2009. Stratigraphy and formation processes of the Upper Pleistocene deposit at Gruta da Oliveira, Almonda karstic system, Torres Novas, Portugal. Geoarchaeology 24 (3), 277–310. https://doi.org/10.1002/gea.20267.

Araújo, A., Lejeune, M., 1995. Gruta do Escoural: Necrópole Neolítica e Arte Rupestre Paleolítica.

Arriolabengoa, M., Iriarte, E., Aranburu, A., Yusta, I., Arnold, L.J., Demuro, M., Arrizabalaga, A., 2018. Reconstructing the sedimentary history of Lezetxiki II cave (Basque Country, northern Iberian Peninsula) using micromorphological analysis. Sediment. Geol. 372, 96–111. https://doi.org/10.1016/j.sedgeo.2018.05.006.

Barbieri, A., 2019. Landscape changes, cave site formation and human occupation during the Late Pleistocene: a geoarchaeological study from the Ach and Lone valleys (Swabian Jura, SW Germany). https://doi.org/10.15496/publikation-26856.

Barbieri, A., Miller, C., 2019. Mikromorphologie. In: Kind, C.-J. (Ed.), LÖWENMENSCH UND MEHR Die Ausgrabungen 2008–2013 in den Altsteinzeitlichen Schichten der Stadel-Höhle im Hohlenstein (Lonetal). Kerns Verlag, pp. 42–44. https://doi.org/10.11588/propylaeum.887.

Barbieri, A., Regala, F.T., Cascalheira, J., Bicho, N., 2023. The sediment at the end of the tunnel: geophysical research to locate the Pleistocene entrance of Gruta da Companheira (Algarve, Southern Portugal). Archaeol. Prospect. 30 (2), 117–134. https://doi.org/10.1002/arp.1881.

Barquín, R., 2015. Estudio ambiental y medidas de conservacion preventiva de las manifestaciones rupestres;de la gruta de Escoural (Alentejo, Portugal). Actuaciones 2010-2012. Almansor | Revista de Cultura 3 (1), 9–50.

Benedetti, M., Haws, J., Bicho, N., Friedl, L., Ellwood, B., 2019. Late Pleistocene site formation and paleoclimate at Lapa do Picareiro, Portugal. Geoarchaeology 34. https://doi.org/10.1002/gea.21735.

Bertran, P., 1993. Deformation-induced microstructures in soils affected by mass movements. Earth Surf. Process. Landf. 18 (7), 645–660. https://doi.org/10.1002/esp.3290180707.

Bertran, P., Texier, J.-P., 1999. Facies and microfacies of slope deposits. Catena 35 (2), 99–121. https://doi.org/10.1016/S0341-8162(98)00096-4.

Blanco, G., Sánchez-Marco, A., Negro, J.J., 2021. Night Capture of Roosting Cave Birds by Neanderthals: An Actualistic Approach [Original Research]. Frontiers in Ecology and Evolution 9. https://doi.org/10.3389/fevo.2021.733062.

Blott, S.J., Pye, K., 2001. GRADISTAT: a grain size distribution and statistics package for the analysis of unconsolidated sediments. Earth Surf. Process. Landf. 26 (11), 1237–1248. https://doi.org/10.1002/esp.261.

Bosch, R., White, W., 2004. Lithofacies and transport of clastic sediments in karstic aquifers. In (pp. 1-22). https://doi.org/10.1007/978-1-4020-5766-3_1.

Boschian, G., 1997. Sedimentology and soil micromorphology of the late Pleistocene and early Holocene deposits of Grotta dell'Edera (Trieste Karst, NE Italy). Geoarchaeology 12 (3), 227–249. https://doi.org/10.1002/(SICI)1520-6548(199705)12:3<227::AID-GEA3>3.0.CO;2-4.

Braillard, L., Guélat, M., Rentzel, P., 2004. Effects of bears on rockshelter sediments at Tanay Sur-les-Creux, southwestern Switzerland. Geoarchaeology 19 (4), 343–367. https://doi.org/10.1002/gea.10123.

Brancaleoni, G., Shnaider, S., Lempart-Drozd, M., Goleń, J., Deput, E., kyzy, S.A., Krajcarz, M.T., 2024. A site formation history of Obishir-5, the earliest Neolithic site in the Fergana Valley (Kyrgyzstan). Archaeol. Anthropol. Sci. 16 (5), 80. https://doi.org/10.1007/s12520-024-01967-w.

Bronk Ramsey, C., 2009. Bayesian analysis of radiocarbon dates. Radiocarbon 51 (1), 337–360. https://doi.org/10.1017/S0033822200033865.

Buccheri, F., BertÈ, D.F., Berruti, G.L.F., Cáceres, I., Volpe, L., Arzarello, M., 2016. Taphonomic analysis on fossil remains from the ciota ciara cave (piedmont, Italy) and new evidence of cave bear and wolf exploitation with simple quartz flakes by neanderthal. Riv. Ital. Paleontol. Stratigr. 122 (3). https://doi.org/10.13130/2039-4942/7674.

Butzer, K.W., 2008. Challenges for a cross-disciplinary geoarchaeology: the intersection between environmental history and geomorphology. Geomorphology 101 (1), 402–411. https://doi.org/10.1016/j.geomorph.2008.07.007.

Canti, M.G., Brochier, J.É., 2017. Plant ash. In: Archaeological Soil and Sediment Micromorphology, pp. 147–154. https://doi.org/10.1002/9781118941065.ch17.

Cardoso, J., Cascalheira, J., 2024. 40,000 years later: what we know about the presence of Neanderthals in Portuguese territory and their extinction. https://doi.org/10.5281/zenodo.12731989.

Carrión, J.S., Riquelme, J.A., Navarro, C., Munuera, M., 2001. Pollen in hyaena coprolites reflects late glacial landscape in southern Spain. Palaeogeogr. Palaeoclimatol. Palaeoecol. 176 (1), 193–205. https://doi.org/10.1016/S0031-0182(01)00338-8.

Carvalhosa, A.B., 1989. Sobre a Faixa Vulcano-Sedimentar de Monfurado (Escoural). Serviços Geologicos de Portugal.

Cobo-Sánchez, L., Rufà, A., Cascalheira, J., 2024. Alternating carnivore and Neanderthal activities at Escoural Cave: insights from the taphonomic and machine learning analysis of leporid remains [Original Research]. Frontiers in Environmental Archaeology 3. https://doi.org/10.3389/fearc.2024.1473266.

Conard, N.J., 2010. Cultural modernity: consensus or conundrum? Proc. Natl. Acad. Sci. 107 (17), 7621–7622. https://doi.org/10.1073/pnas.1001458107.

Conard, N.J., Bolus, M., Münzel, S.C., 2012. Middle Paleolithic land use, spatial organization and settlement intensity in the Swabian Jura, southwestern Germany. Quat. Int. 247, 236–245. https://doi.org/10.1016/j.quaint.2011.05.043.

Courty, M.A., Goldberg, P., Macphail, R., 1989. Soils and Micromorphology in Archaeology. Cambridge: Cambridge.

Craft, C.B., Seneca, E.D., Broome, S.W., 1991. Loss on ignition and kjeldahl digestion for estimating organic carbon and total nitrogen in estuarine marsh soils: calibration with dry combustion. Estuaries 14 (2), 175–179. https://doi.org/10.2307/1351691.

CSIRO, 2000. Huon Estuary study — environmental research for integrated catchment management and aquaculture: final report to fisheries research and development corporation. Marine Laboratories.

Discamps, E., Delagnes, A., Lenoir, M., Tournepiche, J.-F., 2012. Human and Hyena co-occurences in Pleistocene sites : insights from spatial, faunal and lithic analysis at Camiac and La Chauverie (SW France). Journal of Taphonomy 10 (3–4), 291–316.

Dos Santos, M.F., 1964. Vestigios de Pinturas Rupestres Descobertos na gruta do Escoural.

Ekshtain, R., Malinsky-Buller, A., Greenbaum, N., Mitki, N., Stahlschmidt, M.C., Shahack-Gross, R., Hovers, E., 2019. Persistent Neanderthal occupation of the open-air site of 'Ein Qashish, Israel. PLoS One 14 (6), e0215668. https://doi.org/10.1371/journal.pone.0215668.

Finlay, J.C., Kendall, C., 2007. Stable isotope tracing of temporal and spatial variability in organic matter sources to freshwater ecosystems. In: Stable Isotopes in Ecology and Environmental Science, pp. 283–333. https://doi.org/10.1002/9780470691854.ch10.

Finlayson, C., Brown, K., Blasco, R., Rosell, J., Negro, J.J., Bortolotti, G.R., Rodríguez Llanes, J.M., 2012. Birds of a feather: neanderthal exploitation of raptors and corvids. PLoS One 7 (9), e45927. https://doi.org/10.1371/journal.pone.0045927.

Forbes, M., Bestland, E., Wells, R., Krull, E., 2007. Palaeoenvironmental reconstruction of the Late Pleistocene to early Holocene Robertson Cave sedimentary deposit, Naracoorte, South Australia. Australian Journal of Earth Sciences - AUST J EARTH SCI 54, 541–559. https://doi.org/10.1080/08120090601078388.

Ford, D., Williams, P., 2007. Cave interior deposits. In: Karst Hydrogeology and Geomorphology, pp. 271–320. https://doi.org/10.1002/9781118684986.ch8.

Friesem, D.E., Malinsky-Buller, A., Ekshtain, R., Gur-Arieh, S., Vaks, A., Mercier, N., Hovers, E., 2019. New data from Shovakh cave and its implications for reconstructing middle Paleolithic settlement patterns in the amud drainage, Israel. Journal of Paleolithic Archaeology 2 (3), 298–337. https://doi.org/10.1007/s41982-019-00028-2.

Friesem, D.E., Shimelmitz, R., Schumacher, M.L., Miller, C.E., Kandel, A.W., 2022. A micro-geoarchaeological view on stratigraphy and site formation processes in the middle, upper and epi-paleolithic layers of Sefunim Cave, mt. Carmel, Israel. Archaeol. Anthropol. Sci. 14 (12), 222. https://doi.org/10.1007/s12520-022-01686-0.

Gdh-Afrika, G.D. H.a., 2020. *Gruta do Escoural (interior and exterior) 3D model* [3D model]. https://sketchfab.com/3d-models/gruta-do-escoural-interior-and-exterior-ec231dfb1499451ebfa634b5bb920380.

Gillieson, D., 2021. Caves: Processes, Development and Management, second ed.

Gleixner, G., 2013. Soil organic matter dynamics: a biological perspective derived from the use of compound-specific isotopes studies. Ecol. Res. 28 (5), 683–695. https://doi.org/10.1007/s11284-012-1022-9.

Goldberg, P., Dibble, H., Berna, F., Sandgathe, D., McPherron, S.J.P., Turq, A., 2012. New evidence on Neandertal use of fire: examples from Roc de Marsal and Pech de l'Azé IV. Quat. Int. 247, 325–340. https://doi.org/10.1016/j.quaint.2010.11.015.

Goldberg, P., Holliday, V., Ferring, C., 2001. Earth sciences and archaeology. https://doi.org/10.1007/978-1-4615-1183-0.

Goldberg, P., Laville, H., Meignen, L., Bar-Yosef, O., 2007. Stratigraphy and Geoarchaeological History of Kebara Cave, Mount Carmel. in (Vol. 2, Pp. 49-89).

Goldberg, P., Macphail, R., 2006. Practical and theoretical geoarchaeology. https://doi.org/10.1002/9781118688182.

Goldberg, P., Mandel, R.D., 2008. Caves and rockshelters. In: Pearsall, D.M. (Ed.), Encyclopedia of Archaeology. Academic Press, pp. 966–974. https://doi.org/10.1016/B978-012373962-9.00082-0.

Goldberg, P., Sherwood, S.C., 2006. Deciphering human prehistory through the geoarcheological study of cave sediments. Evol. Anthropol. Issues News Rev. 15 (1), 20–36. https://doi.org/10.1002/evan.20094.

Goldberg, P.S., Nathan, Y., 1975. The phosphate mineralogy of et-Tabun cave, Mount Carmel, Israel. Mineral. Mag. 40 (311), 253–258. https://doi.org/10.1180/minmag.1975.040.311.06.

Gomes, M.V., Gomes, R.V., Santos, M.F.D., 1983. O santuário exterior do Escoural. Sector NE (Montemor-o-Novo, Évora).

Gomes, M.V., Ninitas, J., Borralho, R., 2012. Artefactos líticos do povoado calcolítico do Es-coural (Montemor-o-Novo). In: Almansor.

Grimm, E.C., 2022. 1991-2022: TILIA and TILIA Software [computer Program]. In: Research and Collections Center. Springfield, Version 3.0.3.

Helland, P.E., Huang, P.-H., Diffendal, R.F., 1997. SEM analysis of quartz sand grain surface textures indicates Alluvial/Colluvial origin of the Quaternary "Glacial" Boulder clays at huangshan (Yellow Mountain), east-central China. Quat. Res. 48 (2), 177–186. https://doi.org/10.1006/qres.1997.1916.

Horwitz, L., Goldberg, P., 1989. A study of Pleistocene and Holocene hyena coprolites. J. Archaeol. Sci. 16, 71–94. https://doi.org/10.1016/0305-4403(89)90057-5.

Horwitz, L.K., Smith, P., 1988. The effects of striped hyaena activity on human remains. J. Archaeol. Sci. 15 (5), 471–481. https://doi.org/10.1016/0305-4403(88)90077-5.

Hruban, S., 2019. *New Insight on South Western Iberian Rock Art by Non-Invasive Analytical Approaches: the Cases of Ardales and Escoural Cave* Universidade de Evora (Portugal)]. http://hdl.handle.net/10174/26298.

IPMA, 2022. Normal climatológica 1981–2010: Évora/Cidade (Versão 2.2). Retrieved 15/05/2025 from. https://www.ipma.pt/en/oclima/normais.clima/1981-2010/normalclimate8110.jsp.

Jaubert, J., Verheyden, S., Genty, D., Soulier, M., Cheng, H., Blamart, D., Rouzaud, J.-N., 2016. Early Neanderthal constructions deep in Bruniquel Cave in southwestern France. Nature 534 (7605), 43–44. https://doi.org/10.1038/nature18291.

Jover, L., Effler, T., Buchan, A., Wilhelm, S., Weitz, J., 2014. The elemental composition of virus particles: implications for marine biogeochemical cycles. Nat. Rev. Microbiol. 12, 519–528. https://doi.org/10.1038/nrmicro3289.

Karkanas, P., Bar-Yosef, O., Goldberg, P., Weiner, S., 2000. Diagenesis in prehistoric Caves: the use of minerals that form in situ to assess the completeness of the archaeological record. J. Archaeol. Sci. 27 (10), 915–929. https://doi.org/10.1006/jasc.1999.0506.

Karkanas, P., Goldberg, P., 2013. 6.23 micromorphology of cave sediments. In: Shroder, J.F. (Ed.), Treatise on Geomorphology. Academic Press, pp. 286–297. https://doi.org/10.1016/B978-0-12-374739-6.00120-2.

Karkanas, P., Goldberg, P., 2018. Reconstructing Archaeological Sites: Understanding the Geoarchaeological Matrix. John Wiley & Sons Ltd.

Karkanas, P., Rigaud, J.-P., Simek, J.F., Albert, R.M., Weiner, S., 2002. Ash bones and guano: a study of the minerals and phytoliths in the sediments of Grotte XVI,

Dordogne, France. J. Archaeol. Sci. 29 (7), 721–732. https://doi.org/10.1006/jasc.2001.0742.
Krinsley, D.H., Doornkamp, J.C., 1974. Atlas of Quartz Sand Surface Textures. Cambridge University Press.
Kromer, B., Lindauer, S., Synal, H.-A., Wacker, L., 2013. MAMS – a new AMS facility at the curt-engelhorn-centre for Achaeometry, Mannheim, Germany. Nucl. Instrum. Methods Phys. Res. Sect. B Beam Interact. Mater. Atoms 294, 11–13. https://doi.org/10.1016/j.nimb.2012.01.015.
Lambrecht, G., Mallol, C., 2020. Autofluorescence of experimentally heated bone: potential archaeological applications and relevance for estimating degree of burning. J. Archaeol. Sci.: Reports 31, 102333. https://doi.org/10.1016/j.jasrep.2020.102333.
Larsen, G., Chilingarian, G.V., 2010. Diagenesis in Sediments and Sedimentary Rocks, ume 2. Newnes.
Linares-Matás, G.J., Yravedra, J., 2024. Competing forces: subsistence strategies and human-carnivore interactions during the middle to upper Palaeolithic transition in Northern Iberia. Quat. Sci. Rev. 334, 108703. https://doi.org/10.1016/j.quascirev.2024.108703.
Linseele, V., Riemer, H., Baeten, J., De Vos, D., Marinova, E., Ottoni, C., 2013. Species identification of archaeological dung remains: a critical review of potential methods. Environ. Archaeol. 18 (1), 5–17. https://doi.org/10.1179/1461410313Z.00000000019.
LNEG, 2024. Carta Geológica de Portugal à Escala 1:500 000. Laboratório Nacional de Energia e Geologia. https://geoportal.lneg.pt/mapa/.
Loaiza, J.C., Stoops, G., Poch, R., Casamitjana, M. (Eds.), 2015. Manual de Micromorfología de Suelos y Técnicas Complementarias. Fondo Editorial Pascual Bravo.
Lopes, C., 2013. Middle Pleistocene teeth from Arbreda Cave (Serinyà, northeastern Iberian Peninsula). American Journal of Biological Anthropology 185 (4), e25037. https://doi.org/10.1002/ajpa.25037. The art of Escoural Cave XXV Valcamonica Symposium, Lozano, M., Soler, J., López-Onaindia, D., Solés, A., Julià, R., Ceperuelo, D.,…Soler, N. (2024).
Lozano, M., Soler, J., López-Onaindia, D., Solés, A., Julià, R., Ceperuelo, D., Lorenzo, C., Soler, N., 2024. Middle Pleistocene teeth from Arbreda Cave (Serinyà, northeastern Iberian Peninsula). Am. J. Biol. Anthropol. 185 (4), e25037. https://doi.org/10.1002/ajpa.25037.
Macphail, R., Goldberg, P., 2017. Applied soils and micromorphology in archaeology. https://doi.org/10.1017/9780511895562.
Malaurent, P., Huneau, F., Lastennet, R., Fabre, R., 2004. Etudes Pour la Conservation des Parois de la Grotte d'Escoural-Portugal (Conservation Grottes Ornées No. 2004–24). Centre de Développement des Géosciences Appliquées—CDGA, Bordeaux, France.
Mallol, C., Goldberg, P., 2017. Cave and rock shelter sediments. In: Archaeological Soil and Sediment Micromorphology, pp. 359–381. https://doi.org/10.1002/9781118941065.ch34.
Martín-Perea, D.M., Maíllo-Fernández, J.-M., Marín, J., Arroyo, X., Asiaín, R., 2023. A step back to move forward: a geological re-evaluation of the El Castillo Cave Middle Palaeolithic lithostratigraphic units (Cantabria, northern Iberia). J. Quat. Sci. 38 (2), 221–234. https://doi.org/10.1002/jqs.3473.
Marín-Arroyo, A.B., Geiling, J.-M., Jones, J.R., González Morales, M.R., Straus, L.G., Richards, M.P., 2020. The middle to upper Palaeolithic transition at El Mirón Cave (Cantabria, Spain). Quat. Int. 544, 23–31. https://doi.org/10.1016/j.quaint.2018.06.036.
Mellars, P., 1989. Major issues in the emergence of modern humans. Curr. Anthropol. 30 (3), 349–385. https://doi.org/10.1086/203755.
Mellars, P., French, J.C., 2011. Tenfold population increase in Western Europe at the neandertal–to–modern human transition. Science 333 (6042), 623–627. https://doi.org/10.1126/science.1206930.
Mentzer, S.M., 2014. Microarchaeological approaches to the identification and interpretation of combustion features in prehistoric archaeological sites. J. Archaeol. Method Theor 21 (3), 616–668. https://doi.org/10.1007/s10816-012-9163-2.
Menzies, J., Zaniewski, K., 2003. Microstructures within a modern debris flow deposit derived from Quaternary glacial diamicton—a comparative micromorphological study. Sediment. Geol. 157 (1), 31–48. https://doi.org/10.1016/S0037-0738(02)00193-8.
Meyers, P.A., 1997. Organic geochemical proxies of paleoceanographic, paleolimnologic, and paleoclimatic processes. Org. Geochem. 27 (5), 213–250. https://doi.org/10.1016/S0146-6380(97)00049-1.
Mielgo, C., Yravedra Sainz de los Terreros, J., Álvarez-Alonso, D., de Andrés-Herrero, M., Hevia-Carrillo, A., 2024. Unraveling the interplay between humans and carnivores in El Olivo Cave during the Middle and Upper Paleolithic period (Llanera, Asturias, Spain). Geobios. https://doi.org/10.1016/j.geobios.2024.02.008.
Moclán, A., Huguet, R., Márquez, B., Álvarez-Fernández, A., Laplana, C., Arsuaga, J.L., Baquedano, E., 2023. Identifying activity areas in a neanderthal hunting camp (the Navalmaíllo Rock Shelter, Spain) via spatial analysis. Archaeol. Anthropol. Sci. 15 (4), 44. https://doi.org/10.1007/s12520-023-01746-z.
Morales, J.I., Cebrià, A., Burguet-Coca, A., Fernández-Marchena, J.L., García-Argudo, G., Rodríguez-Hidalgo, A., Fullola, J.M., 2019. The middle-to-upper Paleolithic transition occupations from Cova Foradada (Calafell, NE Iberia). PLoS One 14 (5), e0215832. https://doi.org/10.1371/journal.pone.0215832.
Morley, M.W., 2017. The geoarchaeology of hominin dispersals to and from tropical Southeast Asia: a review and prognosis. J. Archaeol. Sci. 77, 78–93. https://doi.org/10.1016/j.jas.2016.07.009.
Morley, M.W., Goldberg, P., Uliyanov, V.A., Kozlikin, M.B., Shunkov, M.V., Derevianko, A.P., Roberts, R.G., 2019. Hominin and animal activities in the microstratigraphic record from Denisova Cave (Altai Mountains, Russia). Sci. Rep. 9 (1), 13785. https://doi.org/10.1038/s41598-019-49930-3.
Mücher, H., Steijn, H.v., Kwaad, F., 2010. 3 - Colluvial and mass wasting deposits. In: Stoops, G., Marcelino, V., Mees, F. (Eds.), Interpretation of Micromorphological Features of Soils and Regoliths. Elsevier, pp. 37–48. https://doi.org/10.1016/B978-0-444-53156-8.00003-9.
Münzel, S.C., Conard, N.J., 2004. Change and continuity in subsistence during the Middle and Upper Palaeolithic in the Ach Valley of Swabia (south-west Germany). Int. J. Osteoarchaeol. 14 (3–4), 225–243. https://doi.org/10.1002/oa.758.
Nicosia, C., Stoops, G., 2017. Archaeological Soil and Sediment Micromorphology. John Wiley & Sons Ltd. https://doi.org/10.1002/9781118941065.
Otte, M., Silva, A.C.d., 1996. Recherches Préhistoriques à la Grotte d'Escoural, vol. 65. Études et recherches archéologiques de l'Université de Liège, Portugal.
Patrick, E.A.F., 1980. Soils; their Formation, Classification and Distribution. Longman.
Peterson, B.J., Fry, B., 1987. Stable isotopes in ecosystem studies. Annu. Rev. Ecol. Systemat. 18, 293–320. https://doi.org/10.1146/annurev.es.18.110187.001453.
Peyroteo-Stjerna, R., Araújo, A.C., Diniz, M., 2018. The Dead at Escoural Cave (Montemor-o-Novo, Portugal): Early Farmer?S Interactions in south-western Iberian Peninsula.
Phillips, E., 2006. Micromorphology of a debris flow deposit: evidence of basal shearing, hydrofracturing, liquefaction and rotational deformation during emplacement. Quat. Sci. Rev. 25 (7), 720–738. https://doi.org/10.1016/j.quascirev.2005.07.004.
Picin, A., Blasco, R., Arilla, M., Rivals, F., Chacón, M.G., Gómez de Soler, B., Rosell, J., 2020. Short-term neanderthal occupations and carnivores in the Northeast of Iberian peninsula. In: Cascalheira, J., Picin, A. (Eds.), Short-Term Occupations in Paleolithic Archaeology: Definition and Interpretation. Springer International Publishing, pp. 183–213. https://doi.org/10.1007/978-3-030-27403-0_8.
Pinto-Llona, A.C., Estaca, V., Grandal-d'Anglade, A., Romero, A.J., Yravedra, J., 2024. Alternation between humans and carnivores in the occupations of the Mousterian site of Sopeña rock-shelter (Asturias, Spain). Quat. Sci. Rev. 328, 108468. https://doi.org/10.1016/j.quascirev.2023.108468.
Pitarch Martí, A., Zilhão, J., d'Errico, F., Cantalejo-Duarte, P., Domínguez-Bella, S., Fullola, J.M., Ramos-Muñoz, J., 2021. The symbolic role of the underground world among Middle Paleolithic Neanderthals. Proc. Natl. Acad. Sci. 118 (33), e2021495118. https://doi.org/10.1073/pnas.2021495118.
Powers, M.C., 1953. A new roundness scale for sedimentary particles. J. Sediment. Res. 23 (2), 117–119.
Reimer, P.J., Austin, W.E.N., Bard, E., Bayliss, A., Blackwell, P.G., Bronk Ramsey, C., Talamo, S., 2020. The IntCal20 Northern hemisphere radiocarbon age calibration curve (0–55 cal kBP). Radiocarbon 62 (4), 725–757. https://doi.org/10.1017/RDC.2020.41.
Rodríguez, C.F., Rego, P.R., Cortizas, A.M., 1995. Characterization and depositional evolution of Hyaena (Crocuta crocuta) coprolites from La Valina Cave (Northwest Spain). J. Archaeol. Sci. 22 (5), 597–607. https://doi.org/10.1016/S0305-4403(95)80145-6.
Sanz, M., Daura, J., 2018. Carnivore involvement in bone assemblages based on taphonomic and zooarchaeological analyses of Cova del Coll Verdaguer site (Barcelona, Iberian Peninsula). Hist. Biol. 30 (6), 807–820. https://doi.org/10.1080/08912963.2017.1351561.
Sanz, M., Daura, J., Égüez, N., Brugal, J.-P., 2016. Not only hyenids: a multi-scale analysis of Upper Pleistocene carnivore coprolites in Cova del Coll Verdaguer (NE Iberian Peninsula). Palaeogeogr. Palaeoclimatol. Palaeoecol. 443, 249–262. https://doi.org/10.1016/j.palaeo.2015.11.047.
Shahack-Gross, R., Berna, F., Karkanas, P., Weiner, S., 2004. Bat guano and preservation of archaeological remains in cave sites. J. Archaeol. Sci. 31 (9), 1259–1272. https://doi.org/10.1016/j.jas.2004.02.004.
Silva, A.C., Garcês, S., Carpetudo, C., 2023. The discovery of Palaeolithic art in Portugal: the Escoural Cave. In: The Prehistoric Rock Art of Portugal. Routledge, pp. 12–25.
Stewart, M., Andrieux, E., Clark-Wilson, R., Vanwezer, N., Blinkhorn, J., Armitage, S.J., Groucutt, H.S., 2021. Taphonomy of an excavated striped hyena (Hyaena hyaena) den in Arabia: implications for paleoecology and prehistory. Archaeol. Anthropol. Sci. 13 (8), 139. https://doi.org/10.1007/s12520-021-01365-6.
Stoops, G., 2020. Guidelines for analysis and description of soil and regolith thin sections. https://doi.org/10.1002/9780891189763.
Stoops, G., Marcelino, V., Mees, F., 2010. Interpretation of micromorphological features of soils and regoliths. https://doi.org/10.1016/C2009-0-18081-9.
Stratford, D., 2024. Site formation in caves and rockshelters. In: Nikita, E., Rehren, T. (Eds.), Encyclopedia of Archaeology, second ed. Academic Press, pp. 35–43. https://doi.org/10.1016/B978-0-323-90799-6.00095-1.
Talamo, S., Fewlass, H., Maria, R., Jaouen, K., 2021. "Here we go again": the inspection of collagen extraction protocols for 14C dating and palaeodietary analysis. Star: Science & Technology of Archaeological Research 7 (1), 62–77. https://doi.org/10.1080/20548923.2021.1944479.
Tassoni, L., Kromer, B., Friedrich, R., Wacker, L., Cattani, M., Friedrich, M., Talamo, S., 2024. Safe preparation and delivery of graphite targets for 14C analysis: procedures of bravho lab at Bologna university. Radiocarbon 66 (5), 1368–1378. https://doi.org/10.1017/RDC.2023.43.
Varis, A., Miller, C.E., Toniato, G., Janas, A., Conard, N.J., 2022. Using formation processes to explore low-density sites and settlement patterns: a case study from the swabian Jura. Journal of Paleolithic Archaeology 5 (1), 14. https://doi.org/10.1007/s41982-022-00127-7.
Vegas, R., 1968. Sobre la existencia de Precámbrico en la Baja Extremadura. Estud. Geol. 24 (1–2), 85–89.
Vepraskas, M.J., Lindbo, D.L., Stolt, M.H., 2018. Chapter 15 - redoximorphic features. In: Stoops, G., Marcelino, V., Mees, F. (Eds.), Interpretation of Micromorphological

Features of Soils and Regoliths, second ed. Elsevier, pp. 425–445. https://doi.org/10.1016/B978-0-444-63522-8.00015-2.
Villa, P., Roebroeks, W., 2014. Neandertal demise: an archaeological analysis of the modern human superiority complex. PLoS One 9 (4), e96424. https://doi.org/10.1371/journal.pone.0096424.
Vos, C., Don, A., Prietz, R., Heidkamp, A., Freibauer, A., 2016. Field-based soil-texture estimates could replace laboratory analysis. Geoderma 267, 215–219. https://doi.org/10.1016/j.geoderma.2015.12.022.
Wacker, L., Christl, M., Synal, H.A., 2010b. Bats: a new tool for AMS data reduction. Nucl. Instrum. Methods Phys. Res. Sect. B Beam Interact. Mater. Atoms 268 (7), 976–979. https://doi.org/10.1016/j.nimb.2009.10.078.
Wacker, L., Němec, M., Bourquin, J., 2010a. A revolutionary graphitisation system: fully automated, compact and simple. Nucl. Instrum. Methods Phys. Res. Sect. B Beam Interact. Mater. Atoms 268 (7), 931–934. https://doi.org/10.1016/j.nimb.2009.10.067.
Weiner, S., Goldberg, P., Bar-Yosef, O., 1993. Bone preservation in Kebara Cave, Israel using on-site fourier transform infrared spectrometry. J. Archaeol. Sci. 20 (6), 613–627.
White, W.B., 2007. Cave Sediments and Paleoclimate.
Zilhão, J., Angelucci, D.E., Igreja, M.A., Arnold, L.J., Badal, E., Callapez, P., Souto, P., 2020. Last interglacial Iberian Neandertals as fisher-hunter-gatherers. Science 367 (6485), eaaz7943. https://doi.org/10.1126/science.aaz7943.
Zilio, L., Hammond, H., Karampaglidis, T., Sánchez-Romero, L., Blasco, R., Rivals, F., Rosell, J., 2021. Examining Neanderthal and carnivore occupations of Teixoneres Cave (Moià, Barcelona, Spain) using archaeostratigraphic and intra-site spatial analysis. Sci. Rep. 11 (1), 4339. https://doi.org/10.1038/s41598-021-83741-9.
Zingg, T., 1935. Beiträge zür Schotteranalyse. Schweizerische Mineralogische und Petrologische Mitteilungen 15, 39–140.